

A Latent Encoder Coupled Generative Adversarial Network (LE-GAN) for Efficient Hyperspectral Image Super-resolution

Yue Shi, Liangxiu Han*, Lianghao Han, Sheng Chang, Tongle Hu, Darren Dancey

Abstract—Realistic hyperspectral image (HSI) super-resolution (SR) techniques aim to generate a high-resolution (HR) HSI with higher spectral and spatial fidelity from its low-resolution (LR) counterpart. The generative adversarial network (GAN) has proven to be an effective deep learning framework for image super-resolution. However, the optimisation process of existing GAN-based models frequently suffers from the problem of mode collapse, leading to the limited capacity of spectral-spatial invariant reconstruction. This may cause the spectral-spatial distortion on the generated HSI, especially with a large upscaling factor. To alleviate the problem of mode collapse, this work has proposed a novel GAN model coupled with a latent encoder (LE-GAN), which can map the generated spectral-spatial features from the image space to the latent space and produce a coupling component to regularise the generated samples. Essentially, we treat an HSI as a high-dimensional manifold embedded in a latent space. Thus, the optimisation of GAN models is converted to the problem of learning the distributions of high-resolution HSI samples in the latent space, making the distributions of the generated super-resolution HSIs closer to those of their original high-resolution counterparts. We have conducted experimental evaluations on the model performance of super-resolution and its capability in alleviating mode collapse. The proposed approach has been tested and validated based on two real HSI datasets with different sensors (i.e. AVIRIS and UHD-185) for various upscaling factors (i.e. $\times 2$, $\times 4$, $\times 8$) and added noise levels (i.e. ∞ db, 40 db, 80 db), and compared with the state-of-the-art super-resolution models (i.e. HyCoNet, LTTR, BAGAN, SR-GAN, WGAN). Experimental results show that the proposed model outperforms the competitors on the super-resolution quality, robustness, and alleviation of mode collapse. The proposed approach is able to capture spectral and spatial details and generate more faithful samples than its competitors. It has also been found that the proposed model is more robust to noise and less sensitive to the upscaling factor and has been proven to be effective in improving the convergence of the generator and the spectral-spatial fidelity of the super-resolution HSIs.

Index Terms—Hyperspectral image super-resolution, Generative adversarial network, Deep learning.

I. INTRODUCTION

Yue Shi, Liangxiu Han, Darren Dancey are with Department of Computing and Mathematics, Faculty of Science and Engineering, Manchester Metropolitan University, Manchester M1 5GD, UK.

Lianghao Han is with Department of Computer Science, Brunel University, UB8 3PH, UK

Sheng Chang is with State Key Laboratory of Remote Sensing Science, Aerospace Information Research Institute, Chinese Academy of Sciences, Beijing 100101, China.

Tongle Hu is College of Plant Protection, Hebei Agriculture University, Baoding 070001, China

Corresponding author: L. Han (e-mail: l.han@mmu.ac.uk)

THE hyperspectral image (HSI) has been widely used in extensive earth observation applications because of the rich information in its abundant spectral bands. However, due to the cost and hardware limitations of imaging systems, the spatial resolution of HSI decreases when the numerous spectral signals are collected simultaneously [1]–[3]. Due to this drawback, the HSI does not always meet the demands for high-accurate earth observation tasks. The HSI super-resolution aiming to estimate a high-resolution (HR) image from a single low-resolution (LR) counterpart is one of promising solutions. Currently, there are mainly two different approaches for HSI super-resolution: 1) the HSI fusion with the HR auxiliary image (e.g. panchromatic image) and 2) the single HSI super-resolution without any auxiliary information. Generally, the image fusion approach implements the super-resolution using filter-based approaches through integrating the high-frequency details of HR auxiliary image into the target LR HSI [4], [5], such as component substitution [6], [7], spectral unmixing [8], [9], and Bayesian probability [10], [11]. However, this method highly relies on the high-quality auxiliary image with high imaging cost, which limits its practical applications. In contrast, single HSI super-resolution does not need any other prior or auxiliary information, which has greater practical feasibility.

In recent years, the single HSI super-resolution technologies have attracted increasing attention in remotely sensed data enhancement [12]. Particularly, Deep Learning (DL)-based single image super-resolution (SISR) methods have achieved significant performance improvement [13]. The first DL-based method for single image super-resolution was proposed by Dong *et al.* [14], named as the super-resolution convolutional neural network (SRCNN). To recover the finer texture details from low-resolution HSIs with large upscaling factors, Ledig *et al.* [15] proposed a super-resolution generative adversarial network (SRGAN) by introducing a generative adversarial network (GAN). After that, various GAN-based deep learning models have been developed and proven to be effective in improving the quality of image super-resolution [16]–[19].

However, existing GAN-based super-resolution approaches mainly focused on RGB images, in which the reflectance radiance characteristics between the neighbouring spectral channels were not considered in the model training processes. Therefore, using these models for HSI super-resolution directly will lead to the absence of spectral-spatial details in the generated images. For example, Fig.1 shows a comparison between an original high-resolution HSI and its super-

88 resolution HSI counterpart generated from the SRGAN model
 89 [13]. Obvious spectral-spatial distortions can be observed on
 90 the generated super-resolution HSI (see the red and yellow
 91 frames in Fig.1). Mathematically, recovering spectral-spatial
 92 details in super-resolution HSI is an under-determined in-
 93 verse problem in which a large number of plausible details
 94 in the high-resolution image need to be characterised from
 95 low-resolution information. The complexity of this under-
 96 determined issue will exponentially increase with the increased
 97 upscaling factor. With high upscaling factors (e.g. higher than
 98 $8 \times$), the spectral-spatial details of generated super-resolution
 99 HSIs could be distorted.

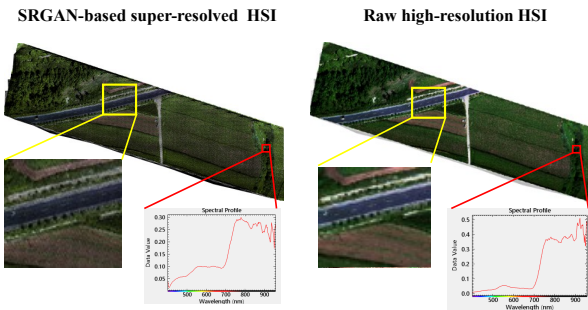


Fig. 1. A comparison between a raw high-resolution (right) HSI and its ($8 \times$) super-resolution HSI (left) counterpart generated by the SRGAN model [15]. The red frames show the spectral distortion occurs in the learning process, and the yellow frames reveal the loss of spatial details in the super-resolution HSI.

1) A novel GAN-based framework has been proposed to improve HSI super-resolution quality. The improvement was achieved from two aspects. Firstly, for improving the spectral-spatial fidelity, a short-term spectral-spatial relationship window (STSSRW) mechanism has been introduced to the generator in order to facilitate spectral-spatial consistency between the generated super-resolution and real high-resolution HSIs in the training process. Secondly, for alleviating the spectral-spatial distortion, a latent encoder has been introduced into the GAN framework as an extra module to make the generator do a better estimation on local spectral-spatial invariance in the latent space.

2) A spectral-spatial realistic perceptual (SSRP) loss has been proposed to guide the optimisation of the under-determined inverse problem and alleviate spectral-spatial mode collapse issues occurred in the HSI super-resolution process, and benefit on retrieving high-quality spectral-spatial details in the super-resolution HSI, especially for high upscaling factors (e.g. $8 \times$). The loss function, SSRP, was able to enforce spectral-spatial invariance in the end-to-end learning process and made the generated super-resolution features closer to the manifold neighbourhood of the targeted high-resolution HSI.

The rest of this work is organised as follows: Section 2 introduces related works on existing GANs-based methods for HSI super resolution tasks; Section 3 details the proposed approach; Section 4 presents experimental evaluation results; Section 5 concludes the work.

II. RELATED WORK

A traditional GAN-based super-resolution model contains two neural networks, a generator producing sample images from low-resolution images and a discriminator distinguishing real and generated images [24]. The generator and discriminator are trained in an adversarial fashion to reach a Nash equilibrium in which the generated super-resolution samples become indistinguishable from real high-resolution samples.

Focusing on the spectral and spatial characteristics of HSI data, various adversarial strategies were proposed to improve the GAN performance on HSI super-resolution tasks [25]. For example, Zhu *et al* [26] proposed a 3D-GAN to improve the generalisation capability of the discriminator in spectral and spatial feature classification with limited ground truth HSI data. Jiang *et al* [27] designed a spectral and spatial block inserted before the GAN generator in order to extract high-frequency spectral-spatial details for reconstructing super-resolution HSI data.

Some methods for improving the overall visual quality of generated HSIs were also proposed through constructing a reliable mapping function between LR and HR HSI pairs. For example, Li *et al* [28] proposed a GAN-based model for multi-temporal HSI data enhancement. In their model, a 3DCNN based upscaling block was used to collect more texture information in the upscaling process. Huang *et al* [29] integrated the residual learning based gradient features between an LR and HR HSI pair with a mapping function in the GAN model, and achieved the HSI super-resolution with an improved spectral and spatial fidelity.

The potential reason behind the spectral-spatial distortion is due to mode collapse in the optimisation process of GANs [20], [21], in which GAN models get stuck in a local minimum and only learn limited modes of data distributions. Some studies have attempted to address mode collapse in GAN models. For instance, Hou *et al.* [22] improved the diversity of the generator in GAN models and attempted to avoid the mode collapse by adding a reverse generating module and an adaptive domain distance measurement module into the GAN framework. Their findings illustrated that these approaches facilitated solving the insufficient diversity of GAN models in remote sensing image super-resolution. Ma *et al.* [23] introduced a memory mechanism into GAN models to save feedforward features and extract local dense features between convolutional layers, which showed some effectiveness in increasing spatial details during the reconstruction procedure.

To benefit the remarkable super-resolution performance from GAN-based models and address the spectral-spatial distortions in HSI super-resolution, in this study, we proposed a novel latent encoder coupled GAN architecture. We treated an HSI as a high-dimensional manifold embedded in a higher dimensional ambient latent space. The optimisation of GAN models was converted to a problem of learning the feature distributions of high-resolution HSIs in the latent space, making the spectral-spatial feature distributions of generated super-resolution HSIs close to those of their original high-resolution counterparts. Our contributions included:

183 The performance of a GAN-based model mainly depends on
184 its generator, its discriminator and loss functions. Therefore,
185 existing studies in improving GAN-based models for HSI
186 resolution focused on their design and optimisation.

187 A. Design of the generator and the discriminator

188 In the generator where LR data are upscaled to a desired
189 size, upscaling filters are the most important components that
190 influence the performance of the generator in term of accuracy
191 and speed [30], [31]. Ledig *et al.* [15] employed a deep
192 ResNet with a skip-connection in the generator to produce
193 super-resolution images with $\times 4$ upscaling factor. Jiang *et al.*
194 [16] proposed an edge-enhancement GAN generator in which
195 a group of dense layers were introduced into the generator
196 in order to capture intermediate high-frequency features and
197 recover the high-frequency edge details of HSI data.

198 In regard to the discriminator, it was found that a deeper net-
199 work architecture had greater potential in discriminating real
200 images from generated ones [15], [32]. For example, Rangneka
201 *et al.* [33] proposed a GAN-based deep convolutional neural
202 network with seven convolutional layers in the discriminator
203 for aerial spectral super-resolution. Arun *et al.* [34] used six
204 3D convolutional filters and three deconvolution filters in the
205 discriminator to discriminate the spectral-spatial features of
206 real HR HSIs from the generated counterparts.

207 In the design of the generator and the discriminator, the
208 computational cost needs to be considered. The upscaling
209 process in the generator can significantly increase the compu-
210 tational cost at the scale of n^2 times for an the upscaling factor
211 of n . Meanwhile, the deep learning-based discriminator always
212 requires a large amount of computational time and memory for
213 extracting and discriminating the high-dimensional non-linear
214 mapping features of input data. More efficient generator and
215 discriminator are required for fast and accurate HSI super-
216 resolution.

217 B. Design of loss functions

218 The loss function plays a very important role in optimising
219 the performance of GAN models [35], [36]. In the traditional
220 GAN model, the generator and the discriminator are trained
221 simultaneously to find a Nash equilibrium to a two-player
222 non-cooperative game. A min-max loss function is used, it
223 is equivalent to minimising Jensen-Shannon (JS) divergence
224 between the distributions of generative data and real samples
225 when the discriminator is optimal. However, the GAN training
226 is hard, and can be slow and unstable. There are some issues
227 in the original GAN model, such as hard to achieve Nash
228 Equilibrium, the problem of low dimensional supports of
229 sample distributions and mode collapse [37], [38]. To facilitate
230 the training stability and address mode collapse problems in
231 the original GAN model, several improved adversarial loss
232 functions were developed, which can be divided into three
233 categories: 1) the pixel-wised loss, 2) the perceptual loss, and
234 3) the probabilistic latent space loss.

235 In the first category, the pixel-wised mean squared error
236 (MSE) loss is commonly used for measuring the discriminative
237 difference between real and generated data in GAN models

[15]. However, the MSE has some issues, such as the loss of
high-frequency details, the over-smoothing problem, and the
sparsity of weights [39]–[41]. Some studies have attempted to
solve these issues. Chen *et al.* [42] introduced a sparse MSE
function into the GAN model in order to measure the high-
frequency information in the spatial attention maps of images,
their results showed that the GAN with the sparse MSE loss
was able to provide more viable segmentation annotations
of images. Zhang *et al.* [43] emphasised that the MSE-loss
always led to an over-smoothing issue in the GAN optimisa-
tion process. Therefore, they introduced a supervised identity-
based loss functions to measure the semantic differences
between pixels in the GAN model. Lei *et al.* [44] attempted
to solve the issue of sparsity of the pixel-wised weights in the
GAN model, and proposed two additional metrics, the edge-
wise KL-divergence and the mismatch rate, for measuring
the sparsity of pixel-wised weights and the wide-value-range
property of edge weights.

256 In the second category, existing studies used different
257 perceptual losses to balance the perceptual similarity, based
258 on high-level features and pixel similarity. Cha *et al.* [45]
259 proposed three perceptual loss functions in order to enforce the
260 perceptual similarity between real and generated images, these
261 functions achieved improved performance on generating high-
262 resolution image with GAN models. Luo *et al.* [46] introduced
263 a novel perceptual loss into the GAN based SR model, named
264 as Bi-branch GANs with soft-thresholding (Bi-GANs-ST), to
265 improve the objective performance. Blau *et al.* [47] proposed
266 a perceptual-distortion loss function in which the generative
267 and perceptual quality of GAN models were jointly quantified.
268 Rad *et al.* [48] proposed a pixel-wise segmentation annotation
269 to optimise the perceptual loss in a more objective way.
270 Their model achieved a great performance in finding targeted
271 perceptual features.

272 In the third category, Bojanowski *et al.* [49] investigated the
273 effectiveness of the latent optimisation for GAN models, and
274 proposed a Generative Latent Optimisation (GLO) strategy for
275 mapping the learnable noise vector to the generated images
276 by minimising a simple reconstruction loss. Compared to
277 a classical GAN, the GLO obtained competitive results but
278 without using the adversarial optimisation scheme which was
279 sensitive to random initialisation, model architectures, and the
280 choice of hyper-parameter settings. Training a stable GAN
281 model is challenging. Therefore, Wasserstein GAN [50] was
282 proposed to improve the stability of learning and reduce mode
283 collapse. The WGAN replaced the discriminator model with
284 a critic which scored the realness of a given image in the
285 probabilistic latent space and was trained using Wasserstein
286 loss. Rather than discriminating between real and generated
287 images (i.e. the probability of a generated image being real),
288 the critic maximises the difference between its prediction for
289 real images and generated images (i.e. predict a "realness"
290 score of a generative image). Gulrajani *et al.* [51] further
291 improved the WGAN training by adding a regularisation term
292 penalising the deviation of the critic's gradient norm with
293 regard to the input, and the model was named as (WGAN-
294 GP).

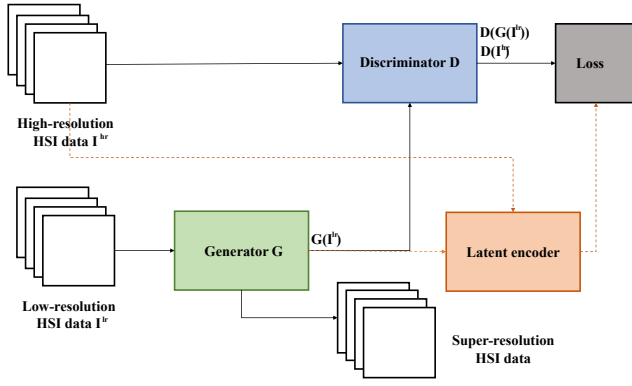


Fig. 2. The architecture of the proposed model: the output from the encoder is used to regularise the loss function

III. THE PROPOSED LE-GAN FOR SINGLE HSI SUPER-RESOLUTION

To address the challenge of spectral-spatial distortions caused by mode collapse during the optimisation process, we proposed a novel GAN model coupled with a latent encoder, named as LE-GAN. In the proposed framework, the optimised generator and discriminator were designed to improve the super-resolution performance and reduce the computational complexity. Inspired by the encoder coupled GAN [52], [53], we developed a latent encoder embedded into our GAN framework to facilitate the generator to achieve a better approximation on feature maps, in order to generate ideal super-resolution results. In addition, we designed a spectral-spatial realistic perceptual (SSRP) loss function in order to optimise the under-determined inverse problem by providing a trade-off between aligning the distributions of generated super-resolution and targeted high-resolution HSIs and increasing the spectral-spatial consistency between them.

A. Model architecture

We have made two major changes to the traditional GAN framework: 1) proposed an improved generator, denoted as G , with a simplified ResNet structure, and 2) introduced a latent encoder, denoted as L_E , into the GAN framework. The network architecture is shown in Fig.2. It consists of a generator, a discriminator and an encoder.

1) *The architecture of the generator model G* : To improve the spectral-spatial reconstruction quality with low distortion and reduce the computational complexity, a short-term spectral-spatial relationship window (STSSRW) derived generator was proposed, denoted as G in our GAN framework. The architecture of the proposed generator G is shown in Fig.3. It serves three functions: low-resolution spectral-spatial feature extraction, STSSRW, and super-resolution HSI reconstruction.

Firstly, for the low-resolution spectral-spatial feature extraction, a 3D convolutional filter is introduced. Unlike traditional RGB image super-resolution approaches that use 2D convolutional filters for spatial feature extraction, the HSI super-resolution requires processing continuous spectral channels and capturing spectral-spatial joint features from a data cube. Therefore, a 3D convolutional filter is a better choice for

modelling both the spectral correlation characteristics and spatial non-local self-similarity. In this study, the convolutional kernel is set to $16 \times 16 \times b$ for a b band HSI input. Nah *et al.* [54] found that the batch normalisation (BN) layer would normalise the features and get rid of the range flexibility for upscaling features. Therefore, no BN layer is used here to avoid blurring the spectral-spatial information hidden in the convolutional features.

Secondly, an STSSRW block is designed to exploit the hierarchical spatial-spectral correlation-state denoted as, H , and further to create the local-global features, F , with low spectral-spatial distortion. It aims to learn the local-global relationship between spectral bands in order to selectively enhance informative band features and spectral-spatial diversity, and achieve low image distortion through modelling the inter-dependencies between high-level features.

More specifically, as shown in Fig. 4a, the low-resolution spectral-spatial data will first be sliced with a sliding window, and then fed into the block. For each data slice B^w , a short-term correlation-state H^{w-1} is introduced through the feedback connect to correct the local-global relationship between the current data slice w and the previous data slice $w-1$. Differing from the existing residual connection models that treat the HSI as a whole data cube, the proposed STSSRW approach further divides the data slice B^w into G chunks based on their spectral similarity, that is, $B^w = [BG_1^w, BG_2^w, \dots, BG_G^w]$. Then, the short-term correlation-state H^{w-1} in the STSSRW block are concatenated with each chunk, $B_g^w (g = 1, G)$, with a 1D convolutional operator to update the local-global correlation between the chunks, and a local feature extractor consisting of two ResBlocks (see Fig. 4b) is used to extract the local spectral characteristics in each chunk. The local feature map of the g -th chunk, FG_g^w , can be calculated by:

$$FG_g^w = f_{Res}(f_{Res}(f_{1DConv}(BG_g^w, H^{w-1}))) \quad (1)$$

After that, the local feature maps $FG_g^w (g = 1, G)$ from all of the chunks are concatenated and reconstructed as the global spectral features with an upscaling deconvolutional operator, and then another high-level feature extractor with two ResBlocks is employed to create the local-global features, F^w . In the end, a correlation-state update operator including two 1D convolutional filters and one sigmoid activation layer is used to aggregate the band-wise information and update the correlation-state, H^w , for the next iteration. Here, F^w and H^w can be computed with:

$$F^w = f_{Res}(f_{Res}(f_{Deconv}([FG_1^w, FG_2^w, \dots, FG_G^w]))) \quad (2)$$

$$H^w = f_{Sigmoid}(f_{1DConv}(f_{1DConv}(f_{Deconv}([FG_1^w, FG_2^w, \dots, FG_G^w]))) \quad (3)$$

where $f_{Sigmoid}, f_{Res}, f_{Deconv}, f_{1DConv}$ represent the operations of Sigmoid, Residual Blocks, Deconvolution and 1D convolution, respectively.

Introducing the STSSRW block into the model can not only reduce the spectral dimensionality and computational complexity like normal residual blocks, but also can explore

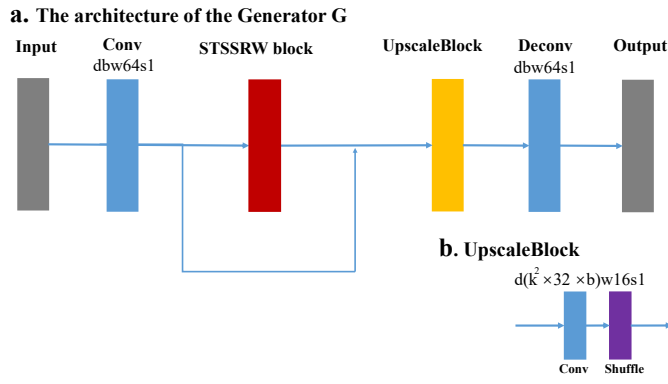


Fig. 3. The architectures of (a) the generator G, (b) the ResBlock component and (c) the UpscaleBlock component. Note: d,w,s are the kernel depth, the kernel width and the stride for a convolutional layer.

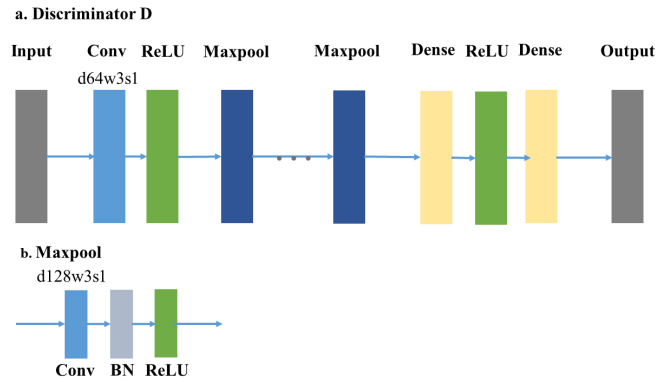


Fig. 5. The architectures of (a) the discriminator, D, and (b) the Maxpool block. Note: d,w and s denote the kernel depth, the kernel width and the stride of a convolutional layer, respectively.

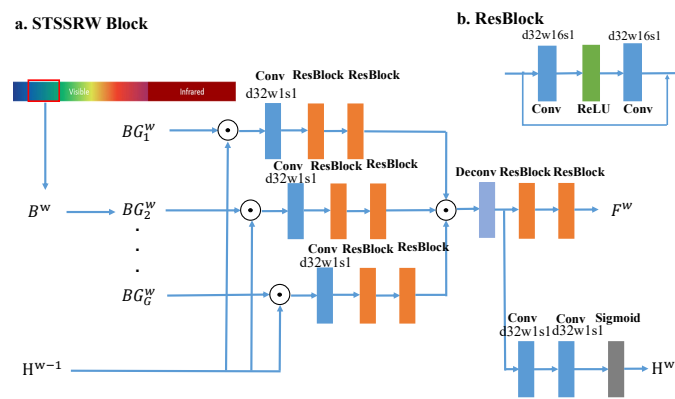


Fig. 4. The architectures of STSSRW block. Note: d,w,s are the kernel depth, the kernel width and the stride for a convolutional layer.

the diversity between adjacent spectral bands within a data slice.

Finally, a skip-connect between the input spectral-spatial feature maps and the output local-global feature maps is conducted to selectively enhance the informative spectral-spatial structure and suppress the distortion. The subsequent results are fed into an UpscaleBlock to generate the super-resolution spectral-spatial details. As shown in Fig.3b, the UpscaleBlock is a combination of a 3D-convolutional filter and a shuffle layer, in which convolutional filters with a depth of 32 are used to exploit $k^2 \cdot 32 \cdot b$ features for an upscaling factor k . The shuffle layer is used to arrange all the features corresponding to each sub-pixel position in a pre-determined order and aggregate them into super-resolution areas. The size of each super-resolution area is $k \times k$. After this operation, the final feature maps with a size of $(k^2 \cdot 32 \cdot b) \times (H/k) \times (W/k)$ will be arranged into the super-resolution feature maps with a size of $32 \cdot b \times H \times W$, where H and W are the height and width of the super-resolution HSI, respectively. At last, a deconvolution filter is used to decode the feature maps in each area, yielding the super-resolution HSI with enhanced spectral-spatial fidelity.

2) *The architecture of the discriminator D:* The architecture of the proposed discriminator, D , as shown in Fig. 5a, adopts an architecture similar to that used in [15]. But, there

is no sigmoid layer in our model, because the latent space optimisation requires the raw membership without compression. Thus, the proposed D mainly contains one convolutional layer, n Maxpool blocks ($n = 8$ is chosen, following the architectural guidelines summarized by [15]) and two dense layers. The Maxpool block is a combination of a convolutional layer, a BN layer, and a ReLU layer (see Fig. 5b). In this study, eight Maxpool blocks are used to reduce the image dimensionality each time and extract the high-level features, and the resultant feature maps are input into two dense layers to obtain a membership distribution of the feature maps for real or generated HSIs.

3) *The architecture of the latent encoder, L_E :* The latent encoder, L_E , is developed and introduced to the GAN architecture for preventing mode collapse by mapping the generated spectral-spatial features from the image space to the latent space and produces the latent regularisation components in the learning process.

Mathematically, the spectral-spatial features of HSI data, I , generated by the latent encoder, $L_E(I)$, can be decomposed with the singular value decomposition as:

$$L_E(I) = U \times \gamma \times V^T \quad (4)$$

where, U and V are the left and right singular vectors of $L_E(I)$, respectively, and γ can be expressed as:

$$\gamma = \begin{pmatrix} SSD & 0 \\ 0 & 0 \end{pmatrix}$$

with $SSD = diag\{\lambda_1, \lambda_2, \dots, \lambda_r\}$, the non-zero part of the diagonal matrix after singular value decomposition of HSI data which represents the spectral-spatial distribution (SSD) of the input HSI in the latent space, in which $(\lambda_1 > \lambda_2 > \dots > \lambda_r)$ are no-negative singular values, and r is the rank of the matrix. Ideally, in the latent space, the SSD of the super-resolution HSI should be close to that of real high-resolution HSI. However, when the mode collapse occurs (e.g. the generated spectral-spatial features distribution only matches part of the real spectral-spatial feature distribution in the latent space), SSD will concentrate on the top singular values and the rest singular values would be close to zero. Thus, the rank of SSD of the generated HSI will be lower than that of the real HSI.

To alleviate the mode collapse, we introduce an extra regularisation term in the loss function to consider the similarity measure of SSD of the spectral-spatial features between the generated data and real data in the latent space. It is defined as:

$$L_{latent} = \mathbb{E}_{I^{hr} \sim P_r(I^{hr})} \|\Delta SSD\|_2 \quad (5)$$

where, $\|\cdot\|_2$ denotes L2 norm, and the ΔSSD is defined as:

$$\begin{aligned} \Delta SSD &= SVD(L_E(I^{hr})) - SVD(L_E(I^{sr})) \\ &= SVD(L_E(I^{hr})) - SVD(L_E(G_{\theta_G}(I^{lr}))) \\ &= \text{diag}\{\lambda_1^{hr} - \lambda_1^{sr}, \dots, \lambda_g^{hr} - \lambda_g^{sr}, \dots, \lambda_r^{hr} - \lambda_r^{sr}, 0, \dots, 0\} \end{aligned} \quad (6)$$

where $L_E(I^{hr})$ and $L_E(I^{sr} = G_{\theta_G}(I^{lr}))$ are the outputs from the latent encoder for the real high resolution image, I^{hr} , and the super-resolution image, I^{sr} , generated from low resolution image, I^{lr} , respectively; SVD denotes the singular value decomposition function; $SVD(I^{hr}) = \text{diag}\{\lambda_1^{hr}, \lambda_2^{hr}, \dots, \lambda_g^{hr}, \lambda_{g+1}^{hr}, \dots, \lambda_r^{hr}, 0, \dots, 0\}$ are the singular values of $L_E(I^{hr})$, and $SVD(I^{sr}) = \text{diag}\{\lambda_1^{sr}, \lambda_2^{sr}, \dots, \lambda_g^{sr}, \lambda_{g+1}^{sr}, \dots, \lambda_r^{sr}, 0, \dots, 0\}$ are the singular values of $L_E(I^{sr} = G_{\theta_G}(I^{lr}))$. This latent regularisation term is used to compensate the difference of singular values between real and generated data in the latent space during the optimisation process, which makes the spectral-spatial feature distribution (i.e. singular values) of the generated HSI more closer to the real feature distribution, and further facilitates the diversity of the generated image covers that of the real high-resolution HSI to prevent the singular value degrading and consequently mode collapse.

The architecture of the latent encoder is shown in Fig. 6, which consists of eight convolutional layers with an increasing kernel depth by a factor 2 through different layers from 64 to 512. The striding operation is used to transfer the spectral-spatial features (low-dimensionality) into the latent features (high-dimensionality) once the kernel depth is doubled. The resultant of 512 feature maps are input into two dense layers so that its outputs match the dimension of the latent space.

As shown in Fig. 2, L_E receives signals from the generator, $G(I^{lr})$, and the targeted data, I^{hr} , and outputs their representations in the latent space which then are used to generate the latent regularisation term, L_{latent} , for the loss function in the model optimisation as described in the section below. To make sure that the outputs of L_E and the real high-resolution HSI in the latent space have the same dimension, L_E is pre-trained by real HSI data. This pre-processing also speeds up the formal optimisation process.

B. Model optimisation with spectral-spatial realistic perceptual loss

In this study, we treat a low-resolution image as a low-dimension manifold embedded in the latent space, thus the super-resolution HSI can be generated by the parametrised latent space learnt by the model. Theoretically, the generated super-resolution sample, $G_{\theta_G}(I^{lr})$, from a low-resolution sample, I^{lr} , by the generator will be located in a neighbourhood area of its target, I^{hr} , in the latent space.

Latent encoder L_E

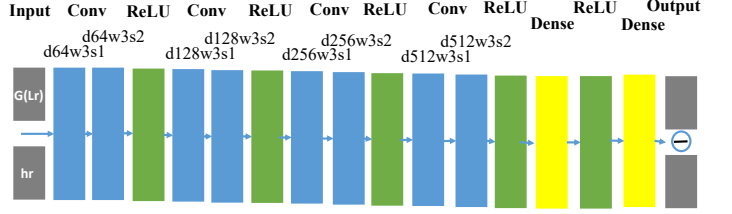


Fig. 6. The architecture of the latent encoder L_E . Note: d,w and s denote the kernel depth, the kernel width and the stride of a convolutional layer, respectively.

Previous studies [36], [42], [43] used the difference between $G_{\theta_G}(I^{lr})$ and I^{hr} as the generator loss function, described as:

$$|G_{\theta_G}(I^{lr}) - I^{hr}|_1 \leq \epsilon \quad (7)$$

However, there are two drawbacks to use this loss function in the HSI super-resolution optimisation process. Firstly, the activated features in the latent space are very sparse. The distance based losses rarely consider the spectral-spatial consistency between $G_{\theta_G}(I^{lr})$ and I^{hr} , which leads to the spectral-spatial distortion in the generated super-resolution HSI results. Secondly, the direct bounding on the difference between $G_{\theta_G}(I^{lr})$ and I^{hr} makes it hard to converge because I^{lr} is usually disturbed by the network impairments or random noise.

In order to overcome the aforementioned drawbacks, we have designed a spectral-spatial realistic perceptual (SSRP) loss to comprehensively measure the spectral-spatial consistency between $G_{\theta_G}(I^{lr})$ and I^{hr} in the latent space. The formula of the SSRP loss is defined as the weighted sum of the spectral contextual loss, the spatial texture loss, the adversarial loss, and a latent regularisation component, and is shown as follows:

$$L_G^{SSRP} = \lambda \cdot L_{spectral} + \eta \cdot L_{spatial} + \sigma \cdot L_{adversarial} + \mu \cdot L_{latent} \quad (8)$$

where $L_{spectral}$ is the spectral contextual loss, $L_{spatial}$ is the spatial texture loss, $L_{adversarial}$ is the adversarial loss, and L_{latent} is the latent regularisation component.

Based on the SSRP loss, the min-max problem in the GAN model can be described as follows:

$$\begin{aligned} \min_{\theta_G} \max_{\theta_D} L(D_{\theta_D}, G_{\theta_G}) &= \min_{\theta_G} \max_{\theta_D} (\lambda \cdot L_{spectral} \\ &+ \eta \cdot L_{spatial} + \sigma \cdot L_{adversarial} + \mu \cdot L_{latent}) \end{aligned} \quad (9)$$

The details of $L_{spectral}$, $L_{spatial}$, $L_{adversarial}$, are provided below; The definition of L_{latent} can be found in Eq. 5.

1) *Spectral contextual loss*: $L_{spectral}$ is designed to measure the spectral directional similarity between $G_{\theta_G}(I^{lr})$ and I^{hr} in the latent space, which is defined as follows:

$$L_{spectral} = \mathbb{E}_z \left\{ -\log \left(\frac{1}{N} \cdot \sum_j \max_i A_{ij} \right) \right\} \quad (10)$$

$$A_{ij} = \frac{e^{1-b_{ij}/n_b}}{\sum_k e^{1-b_{ik}/n_b}} \quad (11)$$

where n_b is the band number of an HSI, and b_{ij} is the normalized spectral directional difference defined as:

$$b_{ij} = \frac{c_{ij}}{\min c_{ij}} \quad (12)$$

where c_{ij} is used to calculate the directional similarity for both the high-level spectral features and the spectral context between the generated HSI, $G_{\theta_G}(I^{lr})$, and the real HSI, I^{hr} , which is defined as:

$$c_{ij} = \frac{(D_{\mu}(G_{\theta_G}(I_{ij}^{lr})) - D_{\mu}(I_{ij}^{hr})) \cdot (G_{\theta_G}(I_{ij}^{lr}) - I_{ij}^{hr})}{\|D_{\mu}(G_{\theta_G}(I_{ij}^{lr})) - D_{\mu}(I_{ij}^{hr})\|_2 \cdot \|G_{\theta_G}(I_{ij}^{lr}) - I_{ij}^{hr}\|_2} \quad (13)$$

where $D_{\mu}(\cdot)$ denotes the feature maps obtained from the convolutional layer before the first Maxpooling layer of the discriminator, D .

2) *Spatial texture loss*: In GAN models, if the loss function only measures the spatial resemblance of the generated and targeted samples, it usually leads to the blurry super-resolution results. In this study, we introduce a spatial texture loss $L_{spatial}$ to measure the texture differences between the feature maps of $G_{\theta_G}(I^{lr})$ and I^{hr} in the latent space. In the $L_{spatial}$, the feature maps of $G_{\theta_G}(I^{lr})$ and I^{hr} before activation are used because they contain more sharp details. $L_{spatial}$ is defined as:

$$L_{spatial} = \mathbb{E}_z \left\{ \frac{1}{W \cdot H} \cdot \sum_{i=1}^W \sum_{j=1}^H \|D_{\phi}(G_{\theta_G}(I_{ij}^{lr})) - D_{\phi}(I_{ij}^{hr})\|_2 \right\} \quad (14)$$

where $D_{\phi}(\cdot)$ denotes the feature maps obtained from the convolutional layer after the last Maxpooling layer of the discriminator D .

3) *Adversarial loss*: Along with the spectral contextual loss and the spatial texture loss, an adversarial loss is introduced to facilitate the generator G in reconstructing the image in the ambient manifold space, and fooling the discriminator network. $L_{adversarial}$ is defined based on the Wasserstein distance [50] between the probability distributions of real data, $P_r(I^{hr})$, and the generated data, $P_g(G_{\theta_G}(I^{lr}))$. Theoretically, $L_{adversarial}$ is strong in alleviating the mode collapse during the training process, because the Wasserstein distance evaluating the similarity between $P_r(I^{hr})$ and $P_g(G_{\theta_G}(I^{lr}))$ rely on the whole samples distributions rather than the individual sample. In other words, there is a penalty would be triggered when the $P_g(G_{\theta_G}(I^{lr}))$ only covers a fraction of $P_r(I^{hr})$, which facilitates the diversity of the generated super-resolution HSI. The goal of $L_{adversarial}$ is to minimise the Wasserstein distance, $W_d(P_r, P_g)$, which is defined as:

$$L_{adversarial} = W_d(P_r, P_g) = \frac{1}{K} \sup_{\|f\|_L < K} \mathbb{E}_{I^{hr} \sim P_r(I^{hr})} [f(I^{hr})] - \mathbb{E}_{I^{lr} \sim P_g(I^{lr})} [f(G_{\theta_G}(I^{lr}))] \quad (15)$$

where f is the K-Lipschitz function. Suppose we have a parametrised family of functions, $\{f_{w_d}\}_{w_d \in W_d}$, that are all

K-Lipschitz for some K , then the $L_{adversarial}$ can be written as:

$$L_D(P_r, P_g) = \max_{w \in W_d} \mathbb{E}_{I^{hr} \sim P_r(I^{hr})} [f_{w_d}(I^{hr})] - \mathbb{E}_{I^{lr} \sim P_g(I^{lr})} [f_{w_d}(G_{\theta_G}(I^{lr}))] \quad (16)$$

where W_d is chosen such that the Lipschitz constant of f_{w_d} is smaller than a constant, K . If the probability densities of $P_r(I^{hr})$ and $P_g(I^{lr})$ satisfy the Lipschitz continuous condition (LCC) [55], there is a solution f_{w_d} . Thus, the discriminator is trained to learn a K-Lipschitz continuous function to help compute the Wasserstein distance. The LCC is a strong prerequisite for calculating $W_d(P_r, P_g)$. Therefore, the parameters, w_d , should lie in a W_d -dimensional manifold in order to meet this constraint.

4) *The latent regularisation component*: In our proposed model, G is a ResNet with global Lipschitz continuity. As described in Section III-A-c, we have introduced a latent encoder, L_E , to compensate the singular values of the spectral-spatial features of I^{lr} to the desired I^{hr} . In addition to the optimisation process, the Lipschitz Continuity Condition (LCC) is employed to enforce the local spectral-spatial invariances of G , and map the latent manifold space to a more regularised latent space in case of mode collapse, described as:

$$\|G_{\theta_G}(I^{lr}) - I^{hr}\|_1 \leq K \times \|L_E(G_{\theta_G}(I^{lr})) - L_E(I^{hr})\|_2 \quad (17)$$

Thus, introducing the regularisation term in the latent space into the loss function (i.e. L_{latent} , see Eq. 5) will make the loss be penalised if the singular values of the spectral-spatial features of a generated super-resolution HSI are updated in a particular direction represented by singular values of SSD). In other words, LLC-derived L_E updating is able to prevent the learning process of each layer from becoming sensitive to the limited direction, which mathematically alleviates the mode collapse, in turn stabilising the optimisation process.

IV. EXPERIMENTAL EVALUATION

In this section, we evaluate the effect of proposed LE-GEN and determined whether it will improve the super-resolution quality and facilitate manifold mapping for solving the problem of mode collapse. Wherein, the developed SSRP loss function plays a key role for both of these prospects. A total of three experiments are designed. The first experiment is to evaluate the optimal parameter combination for the SSRP loss in our proposed model, the second experiment is proposed to evaluate the super-resolution quality, and the last experiment is to evaluate the mode collapse in the model training.

The proposed model was trained and tested on real HSI datasets coming from different sensors. It was also compared with five state-of-the-art super-resolution models, including the hyperspectral coupled network (HyCoNet) [56], the low tensor-train rank (LTTR) network [57], the band attention GAN (BAGAN) [58], the super resolution generative adversarial network (SRGAN) [15], and the Wasserstein GAN (WGAN) [50]. Among them, HyCoNet, LTTR and BAGAN are the state-of-the-art models for HSI super-resolution, while SRGAN and WGAN are the most widely used GAN frameworks for image super-resolution. In order to fit the HSI into

538 the SRGAN and WGAN models, a band-wise strategy was
539 employed [59].

540 A. HSI data descriptions

541 In our experiments, two types of datasets obtained from
542 different sensors were used, one from the public AVIRIS
543 archive, the other from the privately measured UHD-185 data
544 of Guyuan Potato Field (GPF).

545 1) *AVIRIS datasets*: Two publicly available HSIs from
546 the AVIRIS data archive were chosen, including the HSIs
547 of Indian Pines (IP) data and the Kennedy Space Center
548 (KSC). Each of them contains 224 hyperspectral bands from
549 400 ~ 2500nm. The HSIs in the KSC dataset were collected
550 by the Kennedy Space Center, Florida, on March 23, 1996.
551 The spatial resolution was 18 m. The HSIs of IP covered
552 the crop planting areas with the spatial resolution of 20 m in
553 North-Western Indiana, USA. In this study, to keep the spectral
554 consistency between different datasets, only the wavelength
555 ranges from invisible to near-infrared (450 ~ 950nm) were
556 considered in our experiments.

557 2) *UHD-185 dataset*: The UHD-185 dataset contained
558 three privately measured HSIs, denoted as *GPF-1*, *GPF-2*,
559 and *GPF-3*, in Guyuan Potato Field, Hebei, China. Each
560 of the HSIs was collected by the DJI S1000 UAV sys-
561 tem (SZ DJI Technology Co Ltd., Gungdong, China) based
562 UHD-185 Imaging spectrometer (Cubert GmbH, Ulm, Baden-
563 Württemberg, Germany) in 2019. All the images were obtained
564 at a flight height of 30 m, with 220 bands from visible to
565 near-infrared bands between 450 and 950 nm and a spatial
566 resolution close to 0.25m per pixel.

567 B. Evaluation metrics

568 The evaluation metrics include 1) the metrics for evaluating
569 super-resolution quality and robustness and 2) the metrics for
570 evaluating mode collapse of GANs.

571 1) *Evaluation metrics for super-resolution quality and ro-*
572 *bustness assessment*: In total, five spectral-spatial evaluation
573 metrics were employed for the super-resolution quality assess-
574 ment.

575 These five metrics are 1) Information entropy associated
576 peak signal-to-noise (PSNR), 2) Spatial texture associated
577 structural similarity index (SSIM), 3) Perception-distortion
578 associated perceptual index (PI), 4) spectral reality associated
579 spectral angle mapper (SAM) and 5) Spectral consistency
580 associated spectral relative error (SRE). Among them, the
581 PSNR and SSIM were widely used in the evaluation of image
582 quality [60], the larger the score of PSNR or SSIM the higher
583 the image-quality.

The PSNR is defined as:

$$PSNR(I^{hr}, I^{sr}) = 10 \cdot \log_{10}(255^2 / MSE(I^{hr}, I^{sr})) \quad (18)$$

584 where $MSE(I^{hr}, I^{sr})$ is the mean squared error between the
585 real HR HSI, I^{hr} , and the generated HR HSI through super-
586 resolution, I^{sr} . The PSNR goes to infinity as the MSE goes
587 to zero.

The SSIM is defined as:

$$SSIM(I^{hr}, I^{sr}) = l(I^{hr}, I^{sr}) \cdot c(I^{hr}, I^{sr}) \cdot s(I^{hr}, I^{sr}) \quad (19)$$

588 where $l(I^{hr}, I^{sr})$, $c(I^{hr}, I^{sr})$, and $s(I^{hr}, I^{sr})$ are the differ-
589 ence measures for luminance, contrast, and saturation between
590 real and generated HR HSI pairs, respectively. The details can
591 be found in [61].

However, the numerical scores of PSNR and SSIM are
not always correlated well with the subjective image quality.
Therefore, Blau *et al.* [62] proposed an index, PI (Perception
Index), as a compensatory reference for the image quality
evaluation. The lower the PI value is, the higher the perceptual
quality of the image. The PI is defined by two non-referenced
image quality measurements, MA [63] and NIQE [64], de-
scribed as:

$$PI(I^{hr}, I^{sr}) = \frac{1}{2}((10 - MA(I^{hr}, I^{sr})) + NIQE(I^{hr}, I^{sr})) \quad (20)$$

In order to measure the spectral distortion, the spectral
angle mapper(SAM), was used to calculate the average angle
between a super-resolution HSI and its targeted high-resolution
HSI. The SAM is defined as:

$$SAM(I^{hr}, I^{sr}) = \frac{1}{n} \sum arccos\left(\frac{I^{hr} \cdot I^{sr}}{\|I^{hr}\|_2 \cdot \|I^{sr}\|_2}\right) \quad (21)$$

592 where n is the pixel number of the HSI.

To evaluate the pixel-wised spectral reconstruction quality,
the spectral relative error (SRE) was also used as a metric,
defined as:

$$SRE(I^{hr}, I^{sr}) = \left[\frac{1}{n_b} \sum_{i=1}^{n_b} \|(I_i^{hr}, I_i^{sr})\|^2\right]^{\frac{1}{2}} \quad (22)$$

593 where the n_b is the band number of an HSI.

2) *Evaluation metrics for mode collapse of GANs*: Three
metrics for GANs, Inception Score (IS), Frechet Inception
Distance (FID) and non-referenced spectral score (Non-ref
Score), are employed to measure the mode collapse through
monitoring the mode collapse and spectral-spatial distortion
in the model training process [65]–[67]. The IS measures
both the image quality of generated HSIs and their diversity,
reflecting the probability of mode collapse in the model
training process. In GANs, it is desirable for the conditional
probability, $p(I^{hr}|G(I^{lr}))$ to be highly predictable (low en-
tropy), that is, the probability density function is less uniform.
The diversity of the generated image can be measured with
the marginal probability, $p(I^{hr}) = \int p(I^{hr}|G(I^{lr}))dI^{lr}$. The
less uniform (low entropy) the marginal probability is, the less
the diversity of the generated image is. Through computing the
KL-divergence between these two probability distributions, the
IS is computed with the equation below:

$$IS = exp[\mathbb{E}_{I^{lr} \sim p(I^{lr})} [\mathbb{D}_{KL}(p(I^{hr}|G(I^{lr}))||p(I^{hr}))]] \quad (23)$$

The Frechet Inception Distance (FID) score is a metric
calculating the distance between the feature vectors extracted
from real and generated images. It was used to evaluate the
quality of GAN generated images, and a lower FID value
correlates with a higher image quality. More importantly, the
FID is sensitive to mode collapse. Through modelling the
distribution of the features extracted from an intermediate layer
with a multivariate Gaussian distribution, the FID between

the real image and generated images is calculated using the following equation,

$$FID = \|M_{hr} - M_{sr}\|_2^2 + Tr(C_{hr} + C_{sr} - 2(C_{hr} \times C_{sr})^{1/2}) \quad (24)$$

where M_{hr} and M_{sr} refer to the feature-wise means of the real high-resolution HSI and the generated super-resolution HSI in discriminator model, respectively, and C_{hr} and C_{sr} are the covariance matrix for the real and generated feature vectors, respectively.

The non-referenced spectral score (Non-ref Score), which is firstly proposed by [67], is a no-reference assessment method for hyperspectral distortion. It was used to exploit the spectral distortion of GAN generated images. A lower score correlated with a lower reconstructed spectral distortion. The Non-ref Score is calculated by averaging the distances over all intermediate features. The detailed information about Non-ref Score can be referred to [67].

C. Experimental configuration

In our experiments, the raw HSIs were labelled as HR samples. The LR samples were generated by down-sampling the HR samples with three scaling factors, $\times 2$, $\times 4$ and $\times 8$, based on the bi-cubic interpolation approach [68]. For the AVIRIS datasets, the KSC data was used for the model training and test, and the IP data was used for the independent test. For the UHD-185 dataset, the $GPF - 1$ and $GPF - 2$ were used for training and test, and the $GPF - 3$ was used for the independent test. More specifically, for the training/test datasets, the HR HSI was cropped into a series of sub-images with a spatial size of 384×384 , and the corresponding LR data was respectively cropped to 192×192 , 96×96 , and 48×48 . After this operation, a total of 896 HR and LR HSI pairs were generated from the AVIRIS dataset, and 952 HR and LR HSI pairs were generated from the UHD-185 dataset, in which 70% of image pairs were randomly selected as the training set and the rest 30% of image pairs were used as the test set.

The training process was divided into two stages. In the first stage, the discriminator D and the latent encoder L_E were pre-trained over 5,000 iterations on the raw HR HSI dataset to get initial weights. The Adam optimiser was used by setting the forgetting factors, $\beta_1 = 0.9$ and $\beta_2 = 0.999$, a small scalar constant $\epsilon = 10^{-7}$ and the learning rate $= 10^{-4}$ [69]. In the second stage, the discriminator, the generator, and the latent encoder were jointly trained for over 10,000 times, until they converged. The Adam optimiser with the same parameters was used. All of the training were performed on NVIDIA 1080Ti GPUs.

D. Experiment 1: the parameter selection for the SSRP loss function

To achieve an optimal performance, an optimised combination of the parameters in the SSRP loss function Eq.(8), λ , η , σ and μ , needs to be found. In this study, a traversal method was employed to search the optimal parameter combination. These parameters were traversed in the range of 0 to 100 with

TABLE I
THE TOP FIVE COMBINATIONS OF THE PARAMETERS, λ , η , σ AND μ FOR THE SUPER-RESOLUTION HSI GENERATION WITH THE SCALING FACTORS OF $\times 2$, $\times 4$ AND $\times 8$ BASED ON THE VALUES OF SPECTRAL-SPATIAL EVALUATION METRICS AFTER 10,000 ITERATIONS.

Scaling factor	No.	(λ , η , σ , and μ)	PSNR	SSIM	PI	SAM	SRE
$\times 2$	1	(12.8, 12.9, 0.008, 0.015)	31.738	0.982	3.782	5.011	8.383
	2	(12.8, 12.8, 0.009, 0.016)	31.716	0.945	3.884	5.155	8.461
	3	(12.7, 12.8, 0.007, 0.014)	31.712	0.963	3.87	5.115	8.469
	4	(12.8, 12.8, 0.008, 0.014)	31.712	0.943	3.849	5.161	8.482
	5	(12.6, 12.8, 0.006, 0.017)	31.708	0.926	3.876	5.174	8.499
$\times 4$	1	(12.4, 12.4, 0.006, 0.015)	31.417	0.903	3.765	4.942	8.219
	2	(12.4, 12.5, 0.009, 0.014)	31.395	0.901	3.764	5.075	8.267
	3	(12.4, 12.3, 0.007, 0.015)	31.375	0.893	3.765	5.013	8.279
	4	(12.5, 12.8, 0.007, 0.014)	31.359	0.891	3.767	5.017	8.276
	5	(12.5, 12.8, 0.006, 0.017)	31.322	0.898	3.819	5.065	8.331
$\times 8$	1	(12.3, 12.3, 0.005, 0.015)	29.881	0.931	3.672	4.741	8.672
	2	(12.4, 12.3, 0.006, 0.014)	29.851	0.902	3.663	4.828	8.726
	3	(12.4, 12.2, 0.004, 0.014)	29.816	0.885	3.583	4.797	8.753
	4	(12.5, 12.5, 0.005, 0.014)	29.828	0.923	3.617	4.866	8.679
	5	(12.4, 12.6, 0.005, 0.015)	29.791	0.885	3.634	4.817	8.733

a fixed step of 0.001 for the range of 0 to 1, and a fixed step of 0.1 for the range of 1 to 100. The selection of parameter combinations was based on the spectral-spatial quality of generated super-resolution HSIs measured with five evaluation metrics, PSNR, SSIM, PI, SAM, and SRE. Table. I lists the top five parameter combinations and the corresponding values of these metrics for generating the super-resolution HSI with the scaling factors of $\times 2$, $\times 4$ and $\times 8$. It can be observed that all the parameters after optimisation are located in a relatively small range, for example, 12.3–12.8 for λ and η , 0.004–0.009 for σ and 0.014–0.017 for μ . In the following experiments, we employed the average values of the best parameters for various scaling factors, thus, $\lambda = 12.5$, $\eta = 12.5$, $\sigma = 0.0063$, and $\mu = 0.015$.

E. Experiment 2: model robustness and super-resolution quality assessment

To evaluate the robustness and generalizability of the proposed model, we have evaluated our model on both testing datasets and independent datasets.

1) *Model assessment on the testing datasets:* As described in Section IV-C, we divided the dataset into the training and testing datasets. The performance of the proposed model for hyperspectral super-resolution with three upscaling factors ($\times 2$, $\times 4$ and $\times 8$) was evaluated on testing datasets including AVIRIS (KSC) and UHD-185(GPF-1 and GPF-2), and compared with five state-of-the-art competition models. To assess the model robustness to noise, the model was also evaluated on the datasets with artificially added Gaussian white noise at three different levels (∞ , 40db and 80db) to each of the spectral bands of low-resolution HSIs. To facilitate ranking the models in terms of reconstruction quality, five most widely used evaluation metrics, PSNR, SSIM, PI, SAM, and SRE, were chosen. Specifically, PSNR, SSIM and PI were used to measure the spatial reconstructed quality from the aspects of information entropy, spatial similarity, and perception distortion, respectively. The higher PSNR and SSIM scores and the lower PI scores indicate the higher spatial reconstruction quality. In addition, the SAM and SRE scores were used for the spectral distortion measurement from the aspects of spectral angle offset and amplitude difference, respectively. The lower

684 values of SAM and SRE scores indicate the higher spectral
685 reconstruction quality.

686 Table II and Table III provide the average scores of PSNR,
687 SSIM, PI, SAM, and SRE of HSI super-resolution results from
688 the proposed model and its five competitors using the AVIRIS
689 and UHD-185 testing datasets, respectively. In general, the
690 results on both datasets consistently show that the proposed
691 LE-GAN model achieves the highest PSNR and SSIM values
692 and the lowest PI, SAM and SRE values for all three dif-
693 ferent upscaling factors and three added noise levels (see the
694 highlighted values in Table II and Table III). This means that
695 LE-GAN achieves the best spectral and spatial fidelity and
696 super-resolution quality.

697 A more detailed analysis of the results for the model
698 performance evaluation was performed from two aspects: (1)
699 Super-resolution performance under various upscaling factors
700 (2) Model robustness against different noise levels. Since the
701 results in Table II and Table III have the similar patterns for all
702 the models, here we only present the analyses and assessment
703 using the results on AVIRIS data (i.e. Table II):

704 (1) Among three upscaling factors, the LE-GAN based
705 super-resolution with the smallest upscaling factor $\times 2$ and
706 without added noise (i.e. ∞ db) achieves the best spectral and
707 spatial reconstruction quality. The best scores of PSNR, SSIM,
708 PI, SAM, and SRE are 35.513, 0.898, 3.052, 4.207, and 8.379,
709 respectively, which are closer to the real high-resolution HSI
710 (i.e. 35.981 for PSNR, 0.912 for SSIM, 3.011 for PI, 4.142
711 for SAM, and 8.019 for SRE), compared to its competitors.
712 The similarities (i.e. the ratio between the super-resolution
713 HSI and the real high-resolution HSI) reach 98.7%, 98.46%,
714 98.66%, 98.45%, and 95.7%, respectively. In addition, for a
715 given added noise level, the spectral and spatial quality of
716 the LE-GAN generated super-resolution HSIs are more stable
717 between the upscaling factors of $\times 2$ and $\times 4$. For example,
718 under the added noise level of 80db, the PSNR, SSIM, PI,
719 SAM and SRE scores are 35.225, 0.835, 3.171, 4.221, and
720 8.839 for $\times 2$ upscaling factor, and increasing the upscaling
721 factor to $\times 4$ only causes the slight changes to these scores
722 which are 34.975, 0.804, 3.364, 4.362 and 9.062, respectively.
723 The consistency ratios (i.e. the ratio between the $\times 2$ and $\times 4$
724 super-resolution HSI) are 99.29%, 96.29%, 94.26%, 96.78%,
725 and 97.54%, respectively. In contrast, a larger performance
726 degradation occurs on the spectral and spatial reconstruction
727 quality of the competitors. For example, with regard to the
728 WGAN, the second best model in terms of PSNR and SSIM,
729 the scores of PSNR, SSIM, PI, SAM, and SRE under non-
730 added noise level are 33.729, 0.826, 3.867, 7.248, 14.152
731 with $\times 2$ upscaling, but change to 30.035, 0.807, 4.476, 7.922,
732 14.361 with $\times 4$ upscaling, showing the performance degrada-
733 tions of 10.95%, 2.3%, 13.6%, 8.5%, and 1.5%, respectively.
734 Although the degradations of PSNR, SSIM, PI, SAM, SRE
735 scores can be observed on all the models for $\times 8$ upscaling,
736 the degradation rate of these scores from the proposed LE-
737 GAN is the smallest. For example, under the non-added noise
738 (∞ db), the SNR, SSIM, PI, SAM, SRE scores of LE-GAN
739 based super-resolution HSIs for $\times 8$ upscaling are 32.078,
740 0.784, 3.988, 4.711 and 8.986, respectively, which are 21.03%,
741 6.76%, 31.4%, 15.9% and 25.4% higher than those based on

742 the second best models (i.e. the WGAN in terms of SSIM
743 (26.591) and the BAGAN in terms of PSNR (26.591), PI
744 (5.814), SAM (5.602), and SRE(12.048)).

745 (2) With regard to the model robustness to noise, the
746 proposed LE-GAN shows the best performance on the spectral
747 and spatial reconstruction for a given upscaling factor in
748 comparison with its competitors, although the degradation is
749 observed with increased noise levels. The smaller the upscaling
750 factor is, the more robust the model is. The most robust results
751 against noise are at the upscaling factor of $\times 2$. Only 3.6%,
752 7.9%, 14.67%, 13.11%. and 7.33% degradations of the PSNR,
753 SSIM, PI, SAM, and SRE scores of LE-GAN-based super-
754 resolution results occur when the added noise level increases
755 from non-added (∞ db) to 40 db (see Table II). In contrast,
756 the added noise-induced degradations to the results from the
757 WGAN (the second best model for $\times 2$ upscaling factor)
758 are much higher, reaching 20.29%, 8.35%, 26.65%, 20.23%,
759 and 21.61%, respectively. In addition, when the upscaling
760 factor increases from $\times 2$ to $\times 8$, the added noise-induced
761 degradations on the PSNR, SSIM, PI, SAM and SRE scores
762 of the LE-GAN super-resolution results are 9.58%, 11.86%,
763 19.42%, 14.02%, and 11.25%, which are acceptable for the
764 super-resolution with a high upscaling factor and high noises.
765 In contrast, a more serious deterioration can be observed in
766 the results from its competitors. For example, the added noise-
767 induced degradations on the PSNR, SSIM, PI, SAM, SRE of
768 the BAGAN-based super-resolution results, the second best
769 model, are 21.72%, 10.57%, 15.6%, 13.45% and 15.05%,
770 respectively, for an upscaling factor of $\times 2$, but change to
771 24.07%, 23.12%, 13.23%, 15.55%, 19.84% for an upscaling
772 factor of $\times 8$.

773 2) *Model assessment on the independent test datasets:* The
774 proposed model has also been evaluated on two independent
775 test datasets, AVIRIS (IP) and UHD-185 (GPF-3), which
776 were not involved in the model training. Fig. 7 illustrates
777 a comparison of five evaluation metrics (PSNR, SSIM, PI,
778 SAM and SRE) between the proposed model and its five
779 competitors. The average value and standard deviation of
780 each metric were calculated based on the measures at three
781 noise levels, ∞ , 80db and 40db. Compared to its competitors,
782 the proposed model achieves the highest average values and
783 lowest standard deviations for PSNR, SSIM, and the lowest
784 average values and the lowest standard deviation for PI, SAM
785 and SRE, across three upscaling factors on both AVIRIS test
786 dataset (see Fig. 7a) and UHD-185 test dataset (see Fig. 7b).
787 That is, the proposed model achieves the best performance on
788 super-resolution. Similar to the evaluation results in Subsection
789 IV-E1, overall the second best model on the independent test
790 datasets is WGAN for the spatial information reconstruction
791 measure (e.g. PSNR, SSIM), and BAGAN for the spectral
792 information reconstruction measure (e.g. SAM, SRE).

793 It can also be observed that the changes of these metrics are
794 relatively small with the increase of the upscaling factor. When
795 the upscaling factor increases from $\times 2$ to $\times 4$, the average
796 values of SSIM, PI, SAM, and SRE from the proposed model
797 almost stay the same; When the upsampling factor increases
798 from $\times 4$ to $\times 8$, the changes of these metrics are much smaller
799 compared to those from its competitors.

TABLE II

A QUANTITATIVE COMPARISON OF HSIS SUPER-RESOLUTION SPECTRAL AND SPATIAL QUALITY IN TERMS OF THE AVERAGE PSNR, SSIM, PI, SAM, SRE SCORES USING THE PROPOSED MODEL AND FIVE COMPETITION MODELS ON TEST DATASETS, AVIRIS (KSC DATA), WITH VARIOUS UPSAMPLING FACTORS AND ADDED NOISE LEVELS. NOTE THAT THE PSNR/SSIM/PI/SAM/SRE SCORES FOR THE KSC DATA (I.E. REAL HIGH-RESOLUTION HSI) ARE 35.981, 0.912, 3.011, 4.142, AND 8.019 RESPECTIVELY. THE HIGHER PSNR, SSIM AND THE LOWER PI, SAM, SRE, THE BETTER THE SPECTRAL AND SPATIAL FIDELITY.

	SNR(db)		HyCoNet	LTTR	BAGAN	SRGAN	WGAN	LE-GAN	
AVIRIS ($\times 2$)	∞	PSNR	31.213	29.495	32.177	32.421	33.729	35.513	
		SSIM	0.792	0.729	0.766	0.809	0.826	0.898	
		PI	4.181	4.269	3.672	4.015	3.867	3.052	
	80	SAM	6.491	6.515	5.485	9.014	7.248	4.207	
		SRE	10.813	10.145	10.476	15.438	14.152	8.379	
		PSNR	28.751	24.981	29.121	30.106	32.945	35.225	
	40	SSIM	0.719	0.735	0.761	0.756	0.808	0.835	
		PI	4.178	4.819	3.766	3.991	4.196	3.171	
		SAM	6.622	7.164	5.961	10.961	7.297	4.221	
	AVIRIS ($\times 4$)	∞	SRE	12.447	11.913	11.216	19.301	17.914	8.839
			PSNR	23.777	23.253	25.187	26.181	26.886	34.223
			SSIM	0.571	0.634	0.685	0.715	0.757	0.827
80		PI	4.751	3.182	4.351	5.489	5.272	3.577	
		SAM	7.591	7.516	6.338	11.177	9.087	4.842	
		SRE	14.574	12.946	12.332	20.028	18.053	9.042	
AVIRIS ($\times 8$)		∞	PSNR	27.216	27.841	29.177	26.105	30.035	35.367
			SSIM	0.774	0.725	0.762	0.799	0.807	0.835
			PI	4.781	4.474	4.291	4.812	4.476	3.061
		80	SAM	6.514	6.533	5.566	9.729	7.922	4.272
			SRE	12.75	10.811	10.641	16.68	14.361	8.431
			PSNR	24.816	25.896	27.048	22.777	28.183	34.975
	40	SSIM	0.559	0.665	0.513	0.524	0.709	0.804	
		PI	4.514	5.889	4.356	5.037	5.101	3.364	
		SAM	6.571	7.031	5.685	11.582	8.926	4.362	
	AVIRIS ($\times 8$)	∞	SRE	13.551	11.562	11.406	17.799	18.321	9.062
			PSNR	21.714	22.669	26.363	25.934	29.093	33.041
			SSIM	0.315	0.651	0.479	0.668	0.604	0.786
80		PI	6.051	6.072	4.854	6.223	5.912	3.376	
		SAM	6.771	7.736	6.268	12.091	10.138	4.443	
		SRE	15.041	13.203	13.114	18.158	18.556	9.383	
AVIRIS ($\times 8$)		∞	PSNR	19.871	21.747	26.591	24.589	25.332	32.078
			SSIM	0.622	0.638	0.718	0.668	0.731	0.784
			PI	6.835	6.322	5.814	6.536	5.902	3.988
		80	SAM	7.69	6.992	5.602	10.179	8.126	4.711
			SRE	14.361	14.302	12.048	16.943	16.092	8.986
			PSNR	17.821	20.402	24.073	20.603	24.369	30.291
	40	SSIM	0.552	0.493	0.692	0.605	0.663	0.775	
		PI	7.421	7.094	6.411	6.942	6.116	4.326	
		SAM	7.72	7.667	6.283	11.499	9.321	4.732	
	AVIRIS ($\times 8$)	∞	SRE	16.361	15.534	13.194	18.213	18.101	9.768
			PSNR	14.84	18.344	20.191	19.532	21.572	29.003
			SSIM	0.316	0.418	0.552	0.511	0.547	0.691
80		PI	7.622	7.954	6.701	7.924	7.366	4.949	
		SAM	9.172	9.061	6.616	12.541	8.525	5.479	
		SRE	18.219	18.836	15.031	19.597	19.598	10.125	

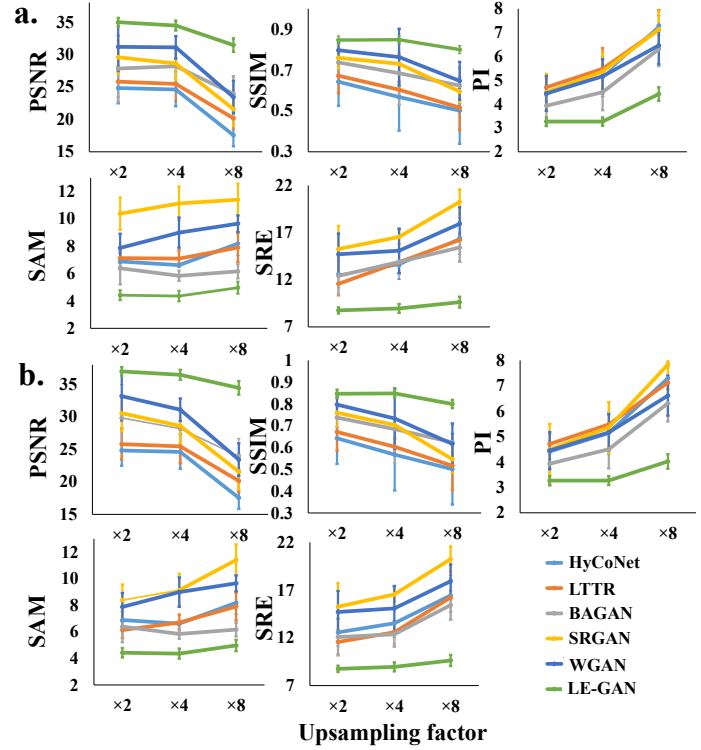


Fig. 7. A comparison of five evaluation metrics (PSNR, SSIM, PI, SAM, and SRE) between the proposed model and its five competitors evaluated on independent test datasets (a) AVIRIS (IP) and (b) UHD-186 (GPF-3). The average values and standard deviations of each metrics are calculated across three different noise levels (∞ , 80db and 40db).

800 These findings suggest that the proposed model overcomes
 801 the drawback associated with spectral-spatial reconstruction
 802 under the noises interferences compared to its competitors.
 803 Moreover, the proposed model is less sensitive to the upscaling
 804 factor, and has a good performance even with a large upscaling
 805 factor (e.g. $\times 8$).

806 3) Visual Analysis of generated super-resolution HSIs with
 807 a large upscaling factor ($\times 8$): To demonstrate the per-
 808 formance improvement of the proposed model in spectral-
 809 spatial fidelity, visual analyses on generated super-resolution
 810 HSI samples have been performed. Fig. 8 displays the results
 811 from independent test datasets (IP and GPF-3). Although
 812 the visualisation results from the proposed method and its
 813 competitors are similar, the image edges from the LE-GAN
 814 are sharper than those from the competitors. For example,
 815 the internal textures of the bare-soil shown as grey in
 816 the false-colour images almost disappear in the generated super-
 817 resolution IP images by the HyCoNet, LTTR, and BAGAN
 818 (the second, third, and fourth images in the first row of Fig. 8).
 819 These findings suggest that the LE-GAN provides improved
 820 spatial quality in general.

821 To further visualise the super-resolution details on spatial

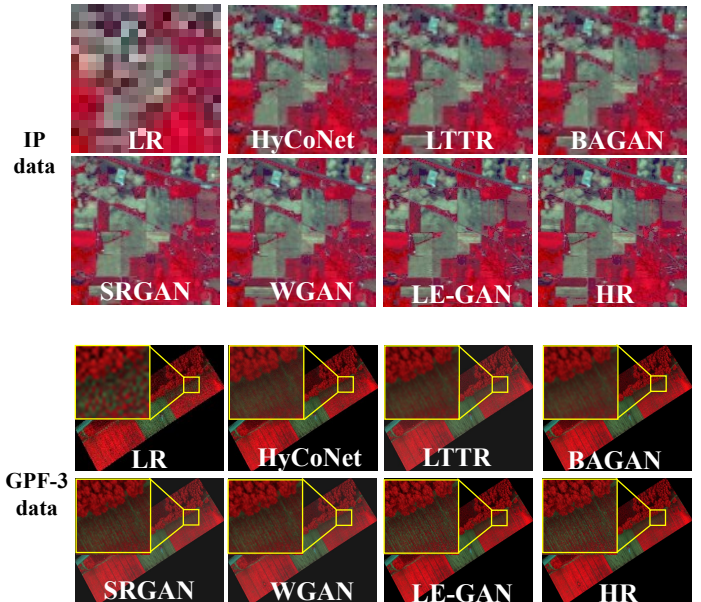


Fig. 8. A sample of super-resolution results ($\times 8$) from our models and its five competitors on independent test datasets

TABLE III

A QUANTITATIVE COMPARISON OF HSI SUPER-RESOLUTION SPECTRAL AND SPATIAL QUALITY IN TERMS OF THE AVERAGE PSNR, SSIM, PI, SAM, SRE SCORES USING THE PROPOSED MODEL AND FIVE COMPETITION MODELS ON TEST DATASETS, UHD-185 (GPF-1 AND GPF-2), WITH VARIOUS UPSCALING FACTORS AND ADDED NOISES. NOTE THAT THE PSNR/SSIM/PI/SAM/SRE SCORES FOR THE KSC DATA (I.E. REAL HIGH-RESOLUTION HSI) ARE 38.915, 0.992, 4.418, 6.942, AND 10.519 RESPECTIVELY. THE HIGHER PSNR AND SSIM AND THE LOWER PI, SAM, AND SRE, THE BETTER THE SPECTRAL AND SPATIAL FIDELITY.

		SNR(db)	HyCoNet	LTTR	BAGAN	SRGAN	WGAN	LE-GAN	
UHD-185 (×2)	∞	PSNR	33.238	32.689	34.642	36.009	37.697	38.575	
		SSIM	0.874	0.875	0.851	0.897	0.879	0.979	
		PI	5.11	5.454	4.799	5.185	5.207	4.323	
	80	SAM	9.174	8.124	7.266	11.848	9.904	6.893	
		SRE	15.755	14.711	12.677	17.341	15.43	10.295	
		PSNR	30.484	29.196	31.913	32.28	35.37	37.625	
	40	SSIM	0.796	0.831	0.841	0.846	0.873	0.922	
		PI	5.911	5.113	5.002	5.341	5.523	4.238	
		SAM	9.331	9.073	7.921	13.05	9.849	6.899	
	UHD-185 (×4)	∞	SRE	14.355	13.441	13.039	20.549	19.842	10.711
			PSNR	28.834	27.137	28.904	29.296	33.752	36.976
			SSIM	0.593	0.622	0.758	0.776	0.833	0.873
80		PI	5.905	6.223	5.636	6.536	6.574	4.592	
		SAM	10.53	10.311	10.172	13.597	11.328	6.508	
		SRE	16.029	14.603	14.523	21.425	19.695	10.823	
UHD-185 (×8)		∞	PSNR	29.855	30.341	34.111	33.285	34.863	38.303
			SSIM	0.717	0.804	0.827	0.861	0.834	0.892
			PI	6.161	5.755	5.309	6.194	5.944	4.391
		80	SAM	9.408	9.187	7.311	12.652	9.937	6.563
			SRE	13.81	12.442	12.208	18.622	15.776	10.005
			PSNR	27.046	27.702	30.396	30.731	33.866	37.061
	40	SSIM	0.661	0.717	0.666	0.813	0.814	0.816	
		PI	6.791	6.995	5.741	6.061	6.276	4.463	
		SAM	9.376	9.909	7.956	13.939	10.09	6.554	
	UHD-185 (×16)	∞	SRE	15.464	14.963	17.128	21.509	19.706	10.361
			PSNR	26.948	26.891	27.917	25.844	32.217	36.556
			SSIM	0.459	0.606	0.567	0.751	0.687	0.731
80		PI	7.521	7.197	6.136	7.621	7.311	4.751	
		SAM	12.679	10.262	9.028	13.99	12.912	6.661	
		SRE	16.518	14.396	14.385	22.221	20.411	10.939	
UHD-185 (×32)		∞	PSNR	22.675	25.375	27.831	27.367	29.012	35.397
			SSIM	0.705	0.688	0.784	0.734	0.821	0.852
			PI	7.908	7.557	6.835	7.863	7.153	5.046
		80	SAM	9.487	9.668	7.827	13.942	10.251	7.104
			SRE	16.378	16.287	13.64	19.011	17.271	10.145
			PSNR	21.879	23.88	26.586	24.029	27.604	33.166
	40	SSIM	0.677	0.549	0.564	0.679	0.755	0.801	
		PI	8.541	8.258	7.426	8.393	7.611	5.649	
		SAM	9.814	10.52	8.931	14.092	12.152	7.669	
	UHD-185 (×64)	∞	SRE	17.627	16.941	15.946	22.224	21.887	11.333
			PSNR	17.819	21.166	23.199	22.251	24.132	31.519
			SSIM	0.419	0.474	0.541	0.591	0.632	0.715
80		PI	8.674	9.154	7.872	9.058	8.755	6.229	
		SAM	13.694	11.175	8.559	15.236	14.212	7.945	
		SRE	20.042	20.604	16.103	25.159	22.086	11.162	

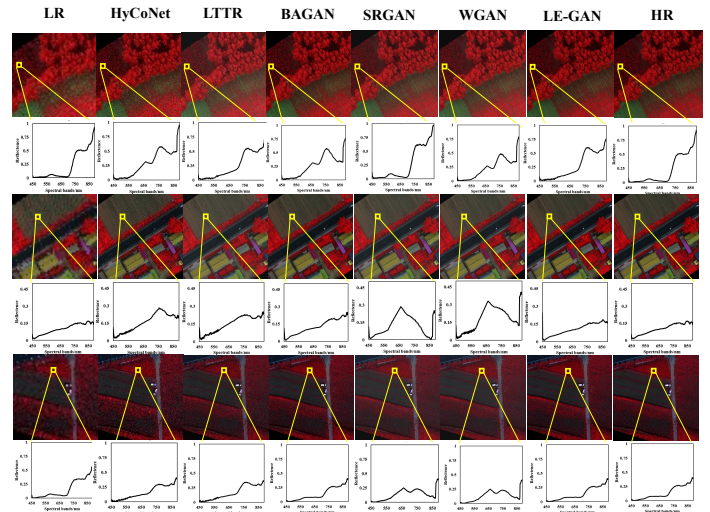


Fig. 9. Detailed spectral analysis on local patches of false colour super resolution (×8) results generated by different models from the independent test dataset, GPF-3. The results in each column from the left to right are for real low resolution (LR) HSI patches, high resolution images generated from models (SRCNN, SRResNet, VDSR, SRGAN, WGAN, and the proposed LRE-GAN), and the corresponding High resolution (HR) HSI patches, respectively.

to 780 nm and lower than 0.25 in the range of 780 to 950 nm, and the deviation is lower than 0.02. All these results suggest that the proposed model provides a better performance in HSI super-resolution without losing the spectral details. The second and third best spectral residuals are achieved by the BAGAN and LTTR, respectively, and the spectral biases in the range of 630 to 950 nm and the average deviations reach 0.029 and 0.041, respectively.

F. Experiment 3: Mode collapse evaluation

Generally, mode collapse mainly happens in the training process when the super-resolution HSI produced by the generator only partially covers the target domain. When the generator learns a type of spectral-spatial pattern that is able to fool the discriminator, it may keep generating this kind of pattern so that the learning process is over-learned. The distance and distribution of the generated super-resolution HSI provide the most direct evidence for determining whether the mode collapse occurs in the generator. In this section, we evaluated the effect of the proposed LE-GAN on alleviating mode collapse from three aspects: 1) a quantitative evaluation on the diversity of the generated super-resolution HSI, based on the distance-derived IS and FID metrics, 2) a smoothness monitoring on the generator iterations during the network training process, and 3) a visualisation of the distributions of the real high-resolution HSI samples and the generated super-resolution samples.

Firstly, the quantitative evaluation for the diversity of the generated super-resolution HSI was conducted on the testing dataset and independent dataset mentioned in Section IV-C. In addition, in order to assess the potential affects of different upscaling factors and added-noise levels on the occurrence of mode collapse, all of the experiments were conducted on three

and spectral fidelity, some representative false-colour composite image patches and the spectral curves of the super-resolved HSI patches from independent test dataset (GPF-3) are shown in Fig. 9. It is obvious that the brightness, contrast, and internal structures of the false-colour images generated by the LE-GAN are more faithful to real HR data. For example, the land cover textures in the LE-GAN generated image (the second image from the right in the second row of images in Fig. 9) are clearer, compared to the images generated by the competitors (e.g. the HyCoNet and LTTR based images) in which the edges of streets are fuzzy. Moreover, the spectral curves from the LE-GAN generated images are more consistent with those from real HR HSI data. For example, the typical vegetation spectral curves in the images generated by the HyCoNet, SRGAN, and WGAN reveal distinct biases in the range of red-edge to near-infrared with real HR data (see the images of the first row in Fig. 9). In contrast, the vegetation spectral curves from the LE-GAN super-resolution are more consistent with those from real HR HSI. A detailed analysis of the spectral residual and standard deviation between the generated HSI and real HR HSI from the independent test dataset is shown in Fig. 10. It can be found that the residual error between the LE-GAN generated HSI and HR HSI is close to zero in the range of 450

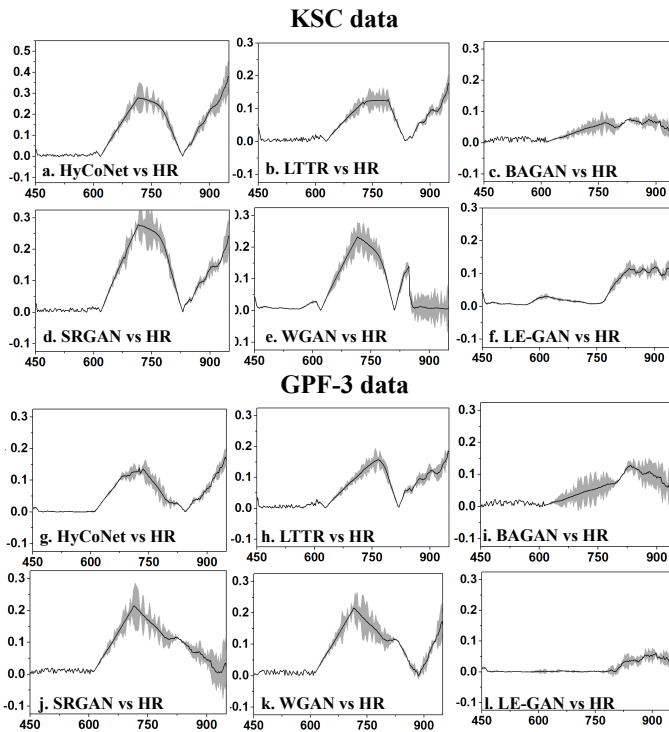


Fig. 10. A spectral residual (the black line) and deviation (the grey shadow) analysis between real HR HSI and the generated super-resolution HSI from different models on the model test dataset (KSC data) and the independent test dataset (GPF-3 data)

TABLE IV
A COMPARISON OF INCEPTION SCORES (IS), FRECHET INCEPTION DISTANCES (FID), AND NON-REFERENCED SPECTRAL SCORE (NON-REF SCORE) OF SUPER-RESOLUTION HSIS GENERATED FROM THE PROPOSED MODEL AND FIVE COMPETITION MODELS USING THE MODEL TEST DATASETS.

Upscaling	SNR	AVIRIS			UHD-185			
		IS	FID	Non-ref Score	IS	FID	Non-ref Score	
∞	2	HyCoNet	11.63	57.37	21.42	9.64	80.15	36.65
		LITR	11	45.55	25.31	8.61	78.67	37.23
		BAGAN	12.26	48.81	18.12	12.01	70.34	31.25
		SRGAN	10.62	53.88	23.25	11.06	74.05	35.52
		WGAN	13.25	24.37	16.25	13.66	49.13	30.21
		LE-GAN	13.46	13.7	11.17	14.69	37.95	19.31
	40	HyCoNet	7.63	58.59	22.26	6.07	96.89	39.92
		LITR	6.79	50.23	23.14	7.99	77.26	31.58
		BAGAN	7.95	49.87	21.02	7.21	83.95	29.92
		SRGAN	6.77	54.59	25.24	6.09	92.06	30.32
		WGAN	11.37	24.45	15.35	8.12	60.83	24.35
		LE-GAN	11.56	15.86	15.21	12.16	40.34	20.82
4	80	HyCoNet	4.35	63.01	26.68	4.05	104.3	41.23
		LITR	5.02	52.42	27.24	4.9	80.12	40.56
		BAGAN	6.32	49.59	25.64	4.79	87.1	36.64
		SRGAN	5.04	60.55	28.66	4.61	94.97	34.25
		WGAN	9.17	26.71	19.92	5.67	76.48	29.25
		LE-GAN	10.16	18.94	17.81	10.13	49.53	25.56
	∞	HyCoNet	9.79	62.14	27.25	8.87	87.65	35.58
		LITR	9.82	49.46	22.45	7.1	86.22	34.45
		BAGAN	11.03	53.51	26.24	10.69	77.25	27.69
		SRGAN	9.64	58.82	25.56	12.78	80.93	31.18
		WGAN	11.14	26.25	19.62	11.87	75.45	25.45
		LE-GAN	12.22	15.37	16.13	14.41	40.76	20.24
8	40	HyCoNet	6.19	63.88	27.98	5.35	105.44	50.2
		LITR	5.91	54.81	24.42	7.08	84.31	32.45
		BAGAN	6.49	53.74	21.25	6.52	91.22	41.57
		SRGAN	5.4	58.94	26.58	5.42	101.1	51.5
		WGAN	9.89	26.71	20.62	7.35	77.32	29.8
		LE-GAN	11.28	17.84	17.99	12.77	43.86	24.85
	∞	HyCoNet	3.83	68.34	35.9	2.91	113.66	55.97
		LITR	4.32	57.13	27.41	4.49	87	38.52
		BAGAN	5.07	54.2	24.58	4.35	94.9	42.51
		SRGAN	4.39	66.08	33.85	3.72	103.29	52.04
		WGAN	7.55	28.64	20.14	5.22	83.75	32.24
		LE-GAN	10.43	19.91	18.38	10.31	50.53	27.25
4	80	HyCoNet	8.44	64.71	34.12	8.04	91.34	48.82
		LITR	8.97	52.06	28.78	6.53	89.81	45.58
		BAGAN	9.33	55.47	25.54	9.31	81.3	38.88
		SRGAN	8.85	61.81	31.15	10.92	84.82	39.98
		WGAN	9.95	26.7	19.25	10.93	79.14	29.28
		LE-GAN	11.67	16.42	18.88	12.11	42.4	24.58
	∞	HyCoNet	4.94	66.62	38.85	4.35	110.48	60.15
		LITR	4.57	57.24	29.82	5.71	88.31	39.94
		BAGAN	5.96	55.75	26.57	5.3	95.53	46.25
		SRGAN	4.54	61.99	33.42	4.1	106.1	52.24
		WGAN	8.89	28	20.24	6	81.33	27.72
		LE-GAN	10.21	19.76	19.98	11.84	45.92	25.58
40	HyCoNet	3.02	71.35	42.12	2.25	119.21	71.15	
	LITR	3.92	59.84	32.42	3.91	91.52	48.82	
	BAGAN	4.32	56.21	31.14	3.12	98.9	53.35	
	SRGAN	3.18	69.28	39.92	2.69	108.21	59.94	
	WGAN	6.47	39.15	25.51	4.51	88.02	38.85	
	LE-GAN	9.6	20.31	20.12	9.03	55.42	27.75	

877 upscaling factors ($\times 2$, $\times 4$ and $\times 8$) with three Gaussian white
 878 noise levels (∞ , 40db and 80db), and compared with five state-
 879 of-the-art competition models. The IS, FID, and Non-ref Score
 880 were used as the evaluation metrics for assessing the diversity
 881 of the super-resolution HSIs and determining the existence of a
 882 mode collapse. A higher IS and lower FID and Non-ref Score
 883 will show the better diversity of the generated super-resolution
 884 HSI and the sign of the alleviation of mode collapse.

885 Table IV lists the IS, FID and Non-ref Score measurements
 886 on the proposed LE-GAN and five selected competitors using
 887 the testing datasets. The evaluation results on AVIRIS and
 888 UHD-185 testing datasets demonstrate that the proposed LE-
 889 GAN model outperforms its competitors in terms of the IS,
 890 FID, and Non-ref score measurements for all three upscaling
 891 factors and added noise combinations (see the highlighted
 892 values in Table IV). They also indicate that the proposed model
 893 has greater performance on alleviating mode collapse issue
 894 occurred in the generated spectral-spatial diversity. The differ-
 895 ences of these measurements between the proposed model
 896 and its competitors are particularly significant for the cases of
 897 low added noise and low upscaling levels. For example, the
 898 proposed LE-GAN achieves the highest IS (13.46 for AVIRIS
 899 data and 14.69 for UHD-185 data), the lowest FID (13.7 for
 900 AVIRIS data and 37.95 for UHD-185 data), and lowest Non-
 901 ref Score (11.17 for AVIRIS data and 19.31 for UHD-185
 902 data) on the datasets with the $\times 2$ upscaling factor and non-
 903 added noise of ∞ SNR.

904 In addition, Table IV also reveals the IS, FID and Non-ref
 905 Score degradations with the increase of upscaling factor and

906 added noise level for all of the models. The comparison of
 907 these degradations can help to explore the model robustness
 908 in preventing the mode collapse issue. Specifically, an average
 909 of 33.6% IS drop, 32.03% FID increase, and 30.68% Non-
 910 ref score increase, are observed from the LE-GAN-based
 911 super-resolution results when increasing the upscaling factor
 912 from $\times 2$ to $\times 8$ and decreasing SNR from from ∞ to 40db.
 913 Meanwhile, the results from the WGAN, the second best
 914 model in terms of super-resolution fidelity (see Section IV-E),
 915 show an average of 59.08% IS drop, 40.97% FID increase,
 916 and 38.78% Non-ref Score increase. These findings suggest
 917 that the proposed LE-GAN achieves the best performance in
 918 preventing mode collapse under the higher upscaling factor
 919 and noise interferences.

920 Table V provides the scores of the IS, FID, and Non-ref
 921 Score from the proposed LE-GAN and its five competitors
 922 using the independent datasets. Similar to the results shown
 923 in Table IV, the results highlighted in Table V illustrate
 924 that the LE-GAN model achieves the best and most robust
 925 performance in terms of IS and FID for all the upscaling
 926 factor and added noise combinations. In the case of a $\times 2$
 927 upscaling factor and non-added noise, the LE-GAN achieves
 928 the best IS, FID, and Non-ref Score measurements (IS of
 929 12.91, FID of 14.95, and Non-ref Score of 9.12 for AVIRIS
 930 and IS of 15.27, FID of 39.22, and Non-ref Score of 19.99

TABLE V
A COMPARISONS OF INCEPTION SCORES (IS), FRECHET INCEPTION DISTANCES (FID), AND NON-REFERENCED SPECTRAL SCORE (NON-REF SCORE) FROM THE PROPOSED MODEL AND FIVE COMPETITION MODELS USING THE INDEPENDENT TEST DATASETS.

Upscaling	SNR	AVIRIS			UHD-185			
		IS	FID	Non-ref Score	IS	FID	Non-ref Score	
∞	40	HCoNet	11.71	59.85	28.81	11.72	81.51	32.52
		LITR	11.58	48.61	23.21	9.71	80.69	32.54
		BAGAN	11.28	52.14	25.52	12.58	72.74	28.84
		SRGAN	10.91	57.35	28.15	13.25	76.32	26.62
		WGAN	12.22	26.26	14.21	14.45	70.71	22.82
		LE-GAN	12.91	14.95	9.12	15.27	39.22	19.99
		HCoNet	7.12	61.86	30.21	6.93	98.2	47.85
		LITR	6.97	53.77	27.82	9.09	79.18	38.45
		BAGAN	8.32	52.03	27.41	8.48	85.1	39.99
		SRGAN	6.72	58.12	29.92	6.7	94.95	46.52
2	80	WGAN	9.89	26.77	17.35	9.31	73.04	29.98
		LE-GAN	10.91	16.51	10.21	13.47	41.66	21.42
		HCoNet	4.07	65.47	34.25	5.1	107.41	58.25
		LITR	5.34	55.72	28.81	7.38	82.46	36.65
		BAGAN	5.34	52.91	26.65	5.56	88.16	39.94
		SRGAN	5.13	63.8	33.51	4.76	97.11	49.95
		WGAN	7.64	27.33	19.24	7.02	79.78	24.94
		LE-GAN	9.18	19.79	12.17	11.4	50.11	22.84
		HCoNet	9.1	65.06	35.52	10.97	89.56	38.85
		LITR	9.62	52.16	28.84	8.53	88.38	40.24
∞	40	BAGAN	9.89	56.53	26.25	11.57	79.97	39.95
		SRGAN	9.46	62.35	31.54	13.65	83.64	33.35
		WGAN	10.41	27.73	18.82	14.56	77.62	27.74
		LE-GAN	10.76	14.8	11.15	14.18	42.2	21.22
		HCoNet	5.49	67.05	38.88	6.27	107.44	59.94
		LITR	6.07	58.44	30.45	7.45	86.43	39.88
		BAGAN	6.68	56.39	29.94	7.26	93.15	43.25
		SRGAN	5.09	62.95	35.52	6.04	103.94	59.95
		WGAN	8.74	28.27	19.94	8.3	79.41	29.99
		LE-GAN	9.94	18.35	12.25	11.84	45.02	22.51
4	80	HCoNet	3.85	71.67	45.25	4.26	116.89	69.94
		LITR	4.7	60.31	36.82	6.37	89.89	48.85
		BAGAN	5.61	57.67	29.94	3.85	96.17	57.74
		SRGAN	4.3	69.84	35.52	4.11	105.25	69.99
		WGAN	6.57	29.18	22.15	6.86	86.78	32.24
		LE-GAN	8.3	21.05	14.21	10.99	54.84	24.21
		HCoNet	8.4	68.3	38.84	9.06	93.81	45.52
		LITR	8.22	55.14	26.68	7.37	92.68	43.32
		BAGAN	9.27	58.74	29.94	10.25	83.57	33.35
		SRGAN	8.31	65.12	36.65	11.83	87.25	39.94
∞	40	WGAN	9.31	28.2	18.74	12.29	81.61	31.15
		LE-GAN	9.8	15.84	12.29	12.82	43.43	23.01
		HCoNet	4.53	70	39.98	5.47	113.15	63.35
		LITR	4.61	60.32	28.84	6.73	90.34	40.41
		BAGAN	5.58	58.78	27.74	5.78	97.65	51.15
		SRGAN	4.51	65.9	35.58	5.13	108.75	57.74
		WGAN	8.81	29.62	21.82	6.85	83.75	32.25
		LE-GAN	9.17	18.05	13.35	10.16	47.84	24.61
		HCoNet	3.37	75.23	42.58	3.33	122.07	82.98
		LITR	4.44	63.42	35.58	4.23	94.2	49.85
8	40	BAGAN	3.98	59.71	31.99	3.96	101.72	55.24
		SRGAN	3.03	73.26	46.65	3.54	110.76	68.95
		WGAN	6.7	31.34	22.25	5.76	90.11	39.98
		LE-GAN	8.77	22.03	15.05	8.2	56.81	26.97

for UHD-185 dataset), with the smallest IS drop (39.1%), FID increase (31.55%), and Non-ref Score increase (30.91%). These results are consistent with the mode collapse assessment reported in Table IV, suggesting that the LE-GAN derived super-resolution HSIs have the best spectral-spatial diversity with alleviated mode collapse.

Secondly, a smoothness monitoring on the generator iteration was used to determine if mode collapse occurred during the training process. According to the results illustrated in Table IV and Table V, the high noise-levels and the large upscaling factors lead to more serious mode collapse. To demonstrate the performance difference between the proposed model and its competitors in alleviating model collapse, a comparison was conducted under a high added noise level (e.g. 40db) and a high upscaling factor (e.g. ×8). Fig. 11 illustrates the IS and FID iterations of the generated HSIs from the proposed LE-GAN and the two best competitors, i.e. WGAN and BAGAN, during the training process. It is obvious that the IS and FID curves from the proposed model are smoother and more stable than those from WGAN or BAGAN, along with the increase of iteration number. Unlike the curves from WGAN or BAGAN, the curves of IS from the proposed mode, LE-GAN, steadily increase and the curves of FID steadily decrease for both AVIRIS and UHD-186 datasets. This indicates that there is no significant mode collapse occurs

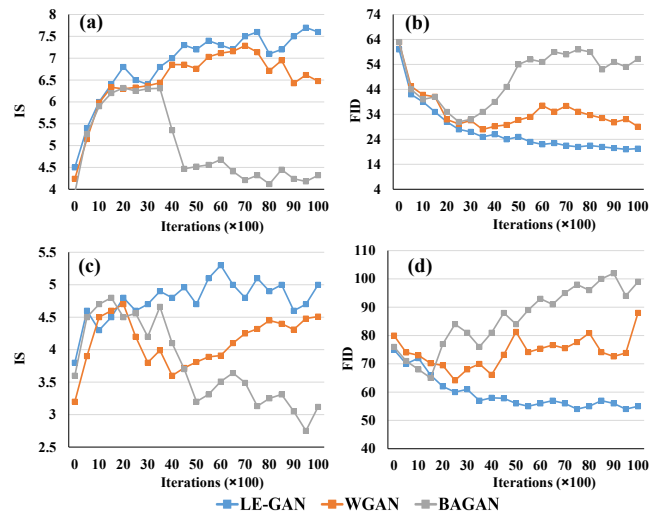


Fig. 11. The changes of IS and FID scores during the training of the proposed LE-GAN and its two best competitors (WGAN and BAGAN). The model training is conducted on (a-b) AVIRIS and (c-d) UHD-186 training dataset with a SNR level of 40db and an upscaling factor of ×8.

during the training of LE-GAN. However, a big drop of IS is observed during the training of BAGAN (e.g. after 3500 iterations, as shown in Fig. 11a) and during the training of WGAN (e.g. after 2000 iterations, as shown in Fig. 11c). Moreover, the curves of FID don't steadily decrease during the training for WGAN or BAGAN. These observations indicate that the mode collapse occurs in the training of representative GAN models (e.g. WGAN and BAGAN), and the proposed model is more effective in alleviating the mode collapse.

Finally, to further understand and assess the performance of the generator model in dealing with the mode collapse issue, the distributions of the real high-resolution HSI (I^{HR}) and the generated super-resolution HSI (I^{SR}) were visualised in the feature space, where the probability densities of the discriminator eigenvalues of I^{HR} and I^{SR} , denoted as $D(I^{HR})$ and $D(I^{SR})$, were used to represent the sample distributions. With I^{HR} and I^{SR} as inputs separately fed into the discriminator D described in Section III-A2, the outputs from the last Maxpool layer, denoted as $D(I^{HR})$ and $D(I^{SR})$, represent the eigenvalues of the inputs I^{HR} and I^{SR} in the high-level discriminating space, and the probability densities of the $D(I^{HR})$ and $D(I^{SR})$ represent the sample distributions of I^{HR} and I^{SR} . The coverage of probability densities between the $D(I^{HR})$ and $D(I^{SR})$ represent the mode similarity of the I^{HR} and I^{SR} to indicate whether model collapse occurs in the generator.

Fig. 12 illustrates that the probability density curves of $D(I^{HR})$ and $D(I^{SR})$ obtained for three GAN models, LE-GAN and its two best competitors, WGAN and BAGAN, through training the models on AVIRIS and UHD-185 datasets with an SNR level of 40db and an upscaling factor of ×8. In comparison with the other two models, the probability density curves of I^{SR} generated by LE-GAN are much closer to those of the real I^{HR} for both AVIRIS (Fig. 12a) and UHD-185 datasets (Fig. 12d). However, the probability density curves of the I^{SR} generated by WGAN (12b and e) and BAGAN (12c

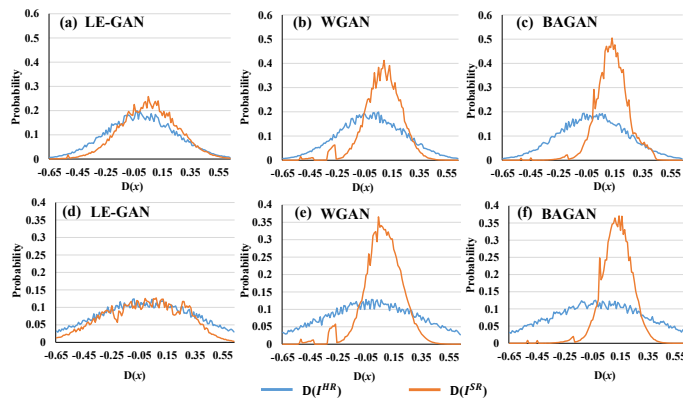


Fig. 12. Statistic distributions of the high-resolution HSI (I^{hr}) and the generated super-resolution HSI (I^{sr}) in the discriminator network (D). We tested the proposed LE-GAN with the two best competitors (i.e. WGAN and BAGAN) on AVIRIS (a-c) and UHD-185 (d-f) test dataset with an SNR level of 40db and an upscaling factor of $\times 8$.

and f) have an obvious tendency shifting towards the right and having a higher peak (i.e. a lower standard deviation). This means the I^{sr} generated by WGAN or BAGAN can be better discriminated from the real I^{hr} by D (i.e. low spectral-spatial fidelity), and the generated I^{sr} only covers the limited spectral-spatial patterns of the real I^{hr} (i.e. existing the mode collapse issue). These observations shows that the proposed model outperforms the competitors in generating diversity of super-resolution samples and alleviating mode collapse.

V. DISCUSSION

The challenge of GANs in improving the spectral and spatial fidelity of HSI super-resolution and addressing the issue of mode collapse is on how to make the generator learn the real spectral-spatial patterns, and meanwhile, prevent the generator from over-learning limited patterns. Since there is no such kinds of constraints in the JS distance based loss functions, the original GAN is hard to generate the high fidelity HSI super-resolution and easy to suffer mode collapse. In this study, we proposed a novel GAN model, named as LE-GAN, through improving the GAN baseline and introducing a new SSRP loss function. The new SSRP loss was used to guide the optimisation and alleviate the spectral-spatial mode collapse issue occurred in the HSI super-resolution process. The model validation and evaluation were conducted using the datasets from two hyperspectral sensors (i.e. AVIRIS and UHD-185) with various upscaling factors ($\times 2$, $\times 4$, and $\times 8$) and added-noises (∞ db, 40db, and 80db). The evaluation results showed that the proposed LE-GAN can achieve high-fidelity HSI super-resolution for relatively high upscaling factors and have a better robustness against noise and better generalizability to various sensors.

A. The ablation analysis of the improved modules

In the proposed model, a total of five different modifications have been made to improve the GAN baseline including: 1) using 3D-convolutional filters in G , 2) adding an UpscaleBlock in G , 3) removing the sigmoid in D , 4) adding a novel

La network, and 5) using a new loss function to optimise the model.

To evaluate the effects of these improvements on the performance of the proposed LE-GAN, we have conducted an ablation analysis in which we gradually substituted the traditional GAN components with the proposed modules and compares their effects based on six evaluation metrics, PSNR, SIM, PI, SAM, SRE, and computing time (CT). Each improvement is an incremental modification to the original GAN model, thus forming five different models: Model 1 to Model 5. The details of the five models and their influences on the six evaluation metrics for the testing datasets (AVIRIS and UHD-185) with $\times 8$ scale factor are presented in Fig.13. The super-resolution results of three example patches are also displayed for the visual comparison.

1) *Model 1: using 3D-convolutional filters in G* : In order to process continuous spectral channels and capture spectral-spatial joint features learning in the ResBlock in G , 3D-convolutional filters are used. Theoretically, this modification is able to extract both the spectral correlation characteristics and spatial texture information.

2) *Model 2: Adding an UpscaleBlock in G* : In a super-resolution network, the most important strategy to improve the performance is to increase the information (e.g. the dimensionality of feature maps) of an LR HSI to match with that of the corresponding HR HSI. However, the traditional approaches increase the feature dimensionality in the entire intermediate layers gradually, which increases the computation complexity and computational cost. In contrast, we proposed an UpscaleBlock to super-resolve the detailed spectral-spatial information only at the end of the generator network (see Fig. 3). This adjustment directly eliminates the need of the computational and memory resources for super-resolution operations. Thus, a smaller filter size can be effectively used in our generator network for the extraction of super-resolution features. The results of Model 2 (the third column in Fig. 13) reveals a performance improvement after adding the UpscaleBlock. Compared to Model 1, the computation time has a 35.1% reduction on average without losing the super-resolution quality, Model 2 even has a better super-resolution quality in terms of PSNR, SSIM, PI, SAM and SRE.

3) *Model 3: Removing the sigmoid function from the discriminator*: In the traditional GAN framework, the sigmoid-activated features often skew the original feature distribution and result in lower reconstructed spectral values. Therefore, in this study, we removed the sigmoid activation in D network for two reasons. Firstly, using the feature before activation can benefit accurate reconstruction of the spectral and spatial features of input. Secondly, the proposed latent space distance requires real feature distribution of the input HSI in the low-dimensional manifold in order to measure the divergence between the generated super-resolution HSI and real HR HIS. This modification, as shown in Model 3 in the fourth column of Fig. 13, contributes to an approximately 7.2% reduction in SAM and 13.9% reduction in SRE. These findings suggest that removing the sigmoid activation can help keep the spectral consistency between the LR and HR HSIs.

1085 4) *Model 4: Adding a newly developed L_E network:* The
 1086 L_E network is developed to produce a latent regularisation
 1087 term, which holds up the manifold space of the generated
 1088 super-resolution HSI so that the dimensionality of the gen-
 1089 erated HSI is consistent with that of real HR HSI. In addition,
 1090 the L_E network makes the divergence of the generated HSI
 1091 and real HSI satisfy the Lipschitz condition for optimisation.
 1092 The generated super-resolution HSI patches from Model 4 (see
 1093 the fifth column of Fig. 13) indicates that, after adding the L_E
 1094 network into the original GAN framework, both SAM and
 1095 SRE have a significant reduction, with a drop of 6.7% and
 1096 15.3%, respectively. Besides, there is a slight improvement on
 1097 the PSNR, SSIM, and PI (the PSNR and SSIM respectively
 1098 increase 2.8% and 1.4%, the PI declines 4.3%). These results
 1099 indicate that the regularisation term produced by the L_E
 1100 network has a great contribution in reconstructing the spectral-
 1101 spatial details consistent with real HR HSI. However, the L_E
 1102 need to occupy a certain amount of computational and memory
 1103 resources, subsequently the computation time increases 15.1%.

1104 5) *Model 5: Using the new loss function to optimise the*
 1105 *model:* The most important contribution of our work is to
 1106 develop a SSRP loss function with a latent regularisation to
 1107 optimise the whole model. Model 5 (see the last column of
 1108 Fig. 13), the final version of the LE-GAN, improves all of
 1109 the evaluation metrics. The increases of PSNR and SSIM are
 1110 5.2% and 12.4%, respectively, while the decreases of SAM
 1111 and SRE are 13.1% and 7.9%, respectively. But, it leads to a
 1112 11.4% increase of computation time. These findings suggest
 1113 that the proposed SSEP loss function with the latent space
 1114 regularisation can boost the performance on measuring the
 1115 divergence of generated HSI and real HSI in both spectral
 1116 and spatial dimensionality.

1117 B. The Evaluation of the loss function

1118 The proposed loss function introducing latent regularisation
 1119 into the Wasserstein loss function optimises the GAN in the
 1120 latent manifold space and addresses the problems of mode
 1121 collapse. In order to verify the effectiveness of the proposed
 1122 loss function, we trained the proposed LE-GAN model with
 1123 three kinds of losses: 1) the traditional JS divergence-based
 1124 loss, 2) the Wasserstein distance-based loss, and 3) the pro-
 1125 posed improved Wasserstein loss with latent regularisation,
 1126 and plotted their loss curves on both the training and validation
 1127 sets in Fig. 14.

1128 It is obvious that the training process of the model with
 1129 a JS divergence-based loss, as shown in Fig. 14a, is un-
 1130 stable and volatile. The reason behind lies in the fact that
 1131 the JS divergence always leads to the supports of P_r and
 1132 P_g disjointing in the low-dimensional manifolds during the
 1133 process of maximising the discriminative capability of D ,
 1134 which causes the gradient fluctuation. On the contrary, the
 1135 Wasserstein distance based loss functions, as shown in Fig.
 1136 14b and c, can improve the stability of learning and lead
 1137 the loss converges to the minimum. This findings is con-
 1138 sistent with Arjovsky *et al.* [50]'s and Ishaan *et al.* [51]'s
 1139 studies. In addition, it is noteworthy that the loss curve of
 1140 the proposed model is more stable and smoother than that of

	1	2	3	4	5
Use 3D-Conv in G	Yes	Yes	Yes	Yes	Yes
Add upscale layer in G	No	Yes	Yes	Yes	Yes
Remove Sigmoid in D	No	No	Yes	Yes	Yes
Use La	No	No	No	Yes	Yes
Use proposed loss function	No	No	No	No	Yes

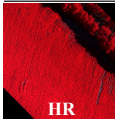
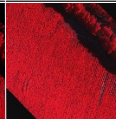
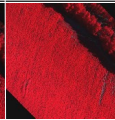
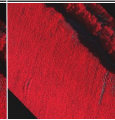
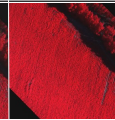

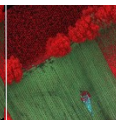
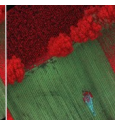
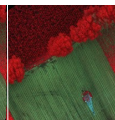
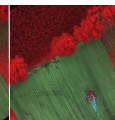
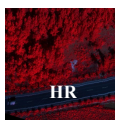
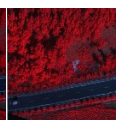
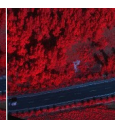
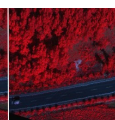

HR					
PSNR/SSIM/PI	31.28/0.87/4.92	32.81/0.88/4.75	32.91/0.88/4.73	33.88/0.91/4.61	35.58/0.99/4.27
SAM/SRE/CT	8.61/13.92/82.4s	/8.41/13.2/54.1s	/7.82/11.23/51.8s	/7.02/10.01/59.3s	/6.81/9.42/62.3s
HR					
PSNR/SSIM/PI	33.81/0.89/4.67	34.81/0.9/4.55	34.91/0.92/4.53	35.88/0.91/4.31	38.81/1.04/4.25
SAM/SRE/CT	/8.72/14.25/90.1s	8.62/13.31/59.9s	/8.21/12.28/54.3s	/7.66/10.4/62.9s	/6.91/9.62/69.84s
HR					
PSNR/SSIM/PI	34.21/0.91/4.9	34.81/0.92/4.81	34.91/0.92/4.77	35.14/0.92/4.39	37.52/1.04/4.11
SAM/SRE/CT	/8.78/14.62/89.3s	/8.71/13.6/56.17s	/8.61/13.02/53.9s	/7.95/10.36/60.4s	/6.99/9.72/63.5s

Fig. 13. The influence of five incremental modifications to the performance of the proposed model in terms of PSNR, SSIM, PI, SRE and computing time (CT). The results in each column (except first column) correspond to one new model with one incremental change to its previous model. The super-resolution results of different models with $\times 8$ scale factor on the testing datasets are illustrated for visual comparison.

1141 the traditional Wasserstein distance-based losses. The theory
 1142 behind is that introducing the latent regularisation terms into
 1143 the training process provides a non-singular support to the
 1144 generated sample sets at the corresponding low-dimensional
 1145 manifolds. It is expected that the Wasserstein distance (i.e.
 1146 $W(P_r, P_g)$) performs better under the condition of the con-
 1147 tinuity and differentiability of the divergence of P_r and P_g .
 1148 With the latent regularisation, the max-min game of LE-GAN
 1149 will yield a probability distribution $P_g(G(I^{lr}))$ in a low-
 1150 dimensional manifold that has a joint support with $P_r(I^{hr})$,
 1151 and the process of minimizing the $W(P_r, P_g)$ will facilitate
 1152 the gradient descent of the trainable parameters in G because
 1153 the valid gradient can be captured from the optimised D in the
 1154 low dimensional manifold. Therefore, the latent regularisation
 1155 derived Wasserstein loss is regarded as a more sensible loss
 1156 function for HSI super-resolution than the JS divergence loss
 1157 and the traditional Wasserstein loss.

1158 The subplots above the learning curve shown in Fig. 14 are
 1159 the images generated in the optimisation process when three
 1160 different losses are used. It is obvious that the super-resolved
 1161 HSI subplots optimised by the JS divergence-based loss (see
 1162 Fig. 14a) do not produce the equivalent quality of spatial
 1163 texture reconstruction as those from the proposed model (see
 1164 Fig. 14b). The proposed latent regularisation term makes the
 1165 dimensionality of the generated HSI manifold more consistent
 1166 with that of the HR HSI in the optimisation process.

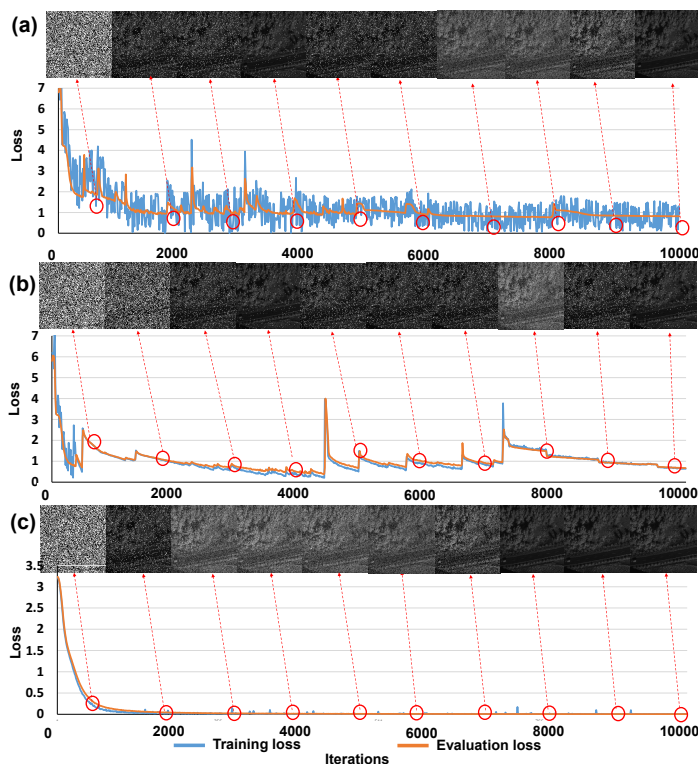


Fig. 14. A comparison of the loss curves during the training of Model 4 using (a) the traditional JS divergence-based loss (b) the Wasserstein distance-based loss, and (c) the proposed improved Wasserstein loss with latent regularisation.

C. Model robustness analysis

Our experimental results have illustrated the great quality scores and robustness for the proposed LE-GAN model. To further analysis the robustness of our proposed model on resisting the complicated down-sampling blurring in practical applications, we discuss the potential of our model generality from two aspects: 1) the theoretical analysis and 2) the additional testing and evaluation on real AVIRIS data products. In the natural conditions, the downsampling blurring is generally caused by two factors, atmospheric effects (e.g. the Gaussian noise and mixed Gaussian noises), and instrumental (sensor) noises (e.g. salt & pepper noise and speckle noise etc). Because the instrumental noises, as part of the internal system errors, are decided by the hardware parameters of a sensor (e.g. the band setting and SNR), here we only discuss the atmospheric effects (i.e. Gaussian noises) under the real natural conditions.

Mathematically, the observed reflectance ($R_{observation}$) can be formulated as the sum of the real reflectance (R_{real}) and noises (N), thus $R_{observation} = R_{real} + N$. Based on our model setting, the spectral-spatial features (SSF) of the $R_{observation}$ will be extracted, and then, the singular value decomposition of spectral-spatial features (SSF) will be conducted in the latent encoder as shown in equation 4. After that, the spectral-spatial distribution (SSD) of SSF used for training the latent regularisation term can be expressed as the sum of the SSD of the real reflectance features (SSD_{real}) and the noise features (SSD_N). Therefore, it is obvious that

the influence of the noise in our model depends on the rank of SSD_N , thus the entropy of the noise, rather than the type of noise. This shows that our model has great potential in tolerating the complicated noise corruptions of HSI. This conclusion is also proven by our experimental results in Section IV-E.

In addition, to further test the generality of our model on more real HSI, we applied our model on the 20 real AVIRIS HSI dataset downloaded from the website (<https://aviris.jpl.nasa.gov/dataportal/>). The results were evaluated in terms of PSNR, SSIM, PI, SAM, SRE, IS, and FID provided in Table S1 of the supplementary. These results are consistent with our experimental results reported in Section IV-E. It concludes that the proposed model has great robustness and generality for the practical applications.

D. Limitations and future works

Benefiting from the self-adaptive latent encoder, the proposed LE-GAN architecture performs better on alleviating the spectral-spatial distortion caused by the mode collapse issue than traditional GAN networks, and the robustness and generalizability of the proposed LE-GAN for HSI super-resolution with large upscaling factor and higher noise levels are better than existing models. The experimental evaluation has illustrated a good spectral-spatial fidelity and diversity of the HSI super-resolution generated by the proposed LE-GAN. Our model will be more adaptive in real applications with different disturbances of HSI super-resolution since the proposed method introduces the STSSRW mechanism into the generator network to enhance the hierarchical spectral-spatial information and ignore the non-hierarchical noises during the upscaling processing. However, there are two limitations should be noticed. First, because our current input data for model training only includes two types of sensors (i.e. UHD-185 and AVIRIS), the direct use of this pre-trained model may lead to limited performance on the unseen images from other sensors with different spectral band settings. Second, in the proposed LE-GAN architecture, an extra latent encoder network will inevitably introduce a lot of parameters and increase the computational complexity. Based on these two limitations, our future work will focus on improving the performance of our model by tackling these two challenges: 1) we will develop a Reinforcement Learning (RL) strategy to utilize the knowledge gained in our pre-trained model in unseen novel tasks, and further test and evaluate the generalization capacities of the proposed adversarial training methods in more complicated and unexpected conditions, 2) Considering the training processes of the generator, discriminator and latent encoder are relatively independent, we will develop a parallel processing strategy to improve the computational efficiency of model training and testing.

VI. CONCLUSION

To address the challenge of spectral-spatial distortions caused by mode collapse during the optimisation process, this work has developed a latent encoder coupled GAN for spectral-spatial realistic HSI super-resolution. In the proposed

GAN architecture, the generator is designed based on an STSSRW mechanism with a consideration of spectral-spatial hierarchical structures during the upscaling process. In addition, a latent regularised encoder is embedded in the GAN framework to map the generated spectral-spatial features into a latent manifold space and make the generator a better estimation of the local spectral-spatial invariances in the latent space. For the model optimisation, a SSRP loss has been introduced to avoid the spectral-spatial distortion in the super-resolution HSI. By using the SSRP loss, both spectral-spatial perceptual differences and adversarial loss in latent space are measured during the optimization process. More importantly, a latent regularisation component is coupled with the optimisation process to maintain the continuity and non-singularity of the generated spectral-spatial feature distribution in the latent space and increase the diversity of the super-resolution features. We have conducted different experimental evaluation in terms of mode collapse and performance. The proposed approach has been tested and validated on AVIRIS and UHD-185 HSI datasets and compared with five state-of-the-art super resolution methods. The results show that the proposed model outperforms the existing methods and is more robust to noise and less sensitive to the upscaling factor. The proposed model is capable of not only generating high quality super-resolution HSIs (both the spatial texture and spectral consistency) but also alleviating mode collapse issue.

ACKNOWLEDGMENT

This research was supported BBSRC (BB/R019983/1), BBSRC (BB/S020969/1). The work is also supported by Newton Fund Institutional Links grant, ID 332438911, under the Newton-Ungku Omar Fund partnership (the grant is funded by the UK Department of Business, Energy, and Industrial Strategy (BEIS)) and the Open Research Fund of Key Laboratory of Digital Earth Science, Chinese Academy of Sciences(No.2019LDE003). For further information, please visit www.newtonfund.ac.uk.

REFERENCES

[1] L. Deng, J. Sun, Y. Chen, H. Lu, F. Duan, L. Zhu, and T. Fan, "M2h-net: A reconstruction method for hyperspectral remotely sensed imagery," *ISPRS Journal of Photogrammetry and Remote Sensing*, vol. 173, pp. 323–348, 2021.

[2] C. Lanaras, J. Bioucas-Dias, S. Galliani, E. Baltsavias, and K. Schindler, "Super-resolution of sentinel-2 images: Learning a globally applicable deep neural network," *ISPRS Journal of Photogrammetry and Remote Sensing*, vol. 146, pp. 305–319, 2018.

[3] F. Palsson, J. R. Sveinsson, and M. O. Ulfarsson, "Multispectral and hyperspectral image fusion using a 3-d-convolutional neural network," *IEEE Geoscience and Remote Sensing Letters*, vol. 14, no. 5, pp. 639–643, 2017.

[4] N. Yokoya, C. Grohnfeldt, and J. Chanussot, "Hyperspectral and multispectral data fusion: A comparative review of the recent literature," *IEEE Geoscience and Remote Sensing Magazine*, vol. 5, no. 2, pp. 29–56, 2017.

[5] P. Ghamisi, B. Rasti, N. Yokoya, Q. Wang, B. Hofle, L. Bruzzone, F. Bovolo, M. Chi, K. Anders, R. Gloaguen *et al.*, "Multisource and multitemporal data fusion in remote sensing: A comprehensive review of the state of the art," *IEEE Geoscience and Remote Sensing Magazine*, vol. 7, no. 1, pp. 6–39, 2019.

[6] J. Qu, Y. Li, and W. Dong, "Hyperspectral pansharpening with guided filter," *IEEE Geoscience and Remote Sensing Letters*, vol. 14, no. 11, pp. 2152–2156, 2017.

[7] G. Khademi and H. Ghassemian, "A multi-objective component-substitution-based pansharpening," in *2017 3rd International Conference on Pattern Recognition and Image Analysis (IPRIA)*. IEEE, 2017, pp. 248–252.

[8] S. E. Brezini, M. S. Karoui, F. Z. Benhalouche, Y. Deville, and A. Ouamri, "Hypersharpening by an nmf-unmixing-based method addressing spectral variability," *IEEE Geoscience and Remote Sensing Letters*, 2021.

[9] C. Lanaras, E. Baltsavias, and K. Schindler, "Hyperspectral super-resolution with spectral unmixing constraints," *Remote Sensing*, vol. 9, no. 11, p. 1196, 2017.

[10] J. A. Benediktsson, G. Cavallaro, N. Falco, I. Hedhli, V. A. Krylov, G. Moser, S. B. Serpico, and J. Zerubia, "Remote sensing data fusion: Markov models and mathematical morphology for multisensor, multiresolution, and multiscale image classification," in *Mathematical Models for Remote Sensing Image Processing*. Springer, 2018, pp. 277–323.

[11] T. Wang, F. Fang, F. Li, and G. Zhang, "High-quality bayesian pansharpening," *IEEE Transactions on Image Processing*, vol. 28, no. 1, pp. 227–239, 2018.

[12] J. M. Bioucas-Dias, A. Plaza, G. Camps-Valls, P. Scheunders, N. Nasrabadi, and J. Chanussot, "Hyperspectral remote sensing data analysis and future challenges," *IEEE Geoscience and remote sensing magazine*, vol. 1, no. 2, pp. 6–36, 2013.

[13] W. Yang, X. Zhang, Y. Tian, W. Wang, J. Xue, and Q. Liao, "Deep learning for single image super-resolution: A brief review," *IEEE Transactions on Multimedia*, vol. 21, no. 12, pp. 3106–3121, 2019.

[14] C. Dong, C. C. Loy, K. He, and X. Tang, "Image super-resolution using deep convolutional networks," *IEEE Transactions on Pattern Analysis and Machine Intelligence*, vol. 38, no. 2, pp. 295–307, 2016.

[15] C. Ledig, L. Theis, F. Huszár, J. Caballero, A. Cunningham, A. Acosta, A. Aitken, A. Tejani, J. Totz, and Z. Wang, "Photo-realistic single image super-resolution using a generative adversarial network," in *Proceedings of the IEEE conference on computer vision and pattern recognition*, 2017, Conference Proceedings, pp. 4681–4690.

[16] K. Jiang, Z. Wang, P. Yi, G. Wang, T. Lu, and J. Jiang, "Edge-enhanced gan for remote sensing image superresolution," *IEEE Transactions on Geoscience and Remote Sensing*, vol. 57, no. 8, pp. 5799–5812, 2019.

[17] B. Lim, S. Son, H. Kim, S. Nah, and K. Mu Lee, "Enhanced deep residual networks for single image super-resolution," in *Proceedings of the IEEE conference on computer vision and pattern recognition workshops*, 2017, Conference Proceedings, pp. 136–144.

[18] X. Wang, K. Yu, S. Wu, J. Gu, Y. Liu, C. Dong, Y. Qiao, and C. Change Loy, "Esrgan: Enhanced super-resolution generative adversarial networks," in *Proceedings of the European Conference on Computer Vision (ECCV)*, 2018, Conference Proceedings, pp. 0–0.

[19] Y. Zhang, Y. Tian, Y. Kong, B. Zhong, and Y. Fu, "Residual dense network for image super-resolution," in *Proceedings of the IEEE conference on computer vision and pattern recognition*, 2018, Conference Proceedings, pp. 2472–2481.

[20] Y. Xiong, S. Guo, J. Chen, X. Deng, L. Sun, X. Zheng, and W. Xu, "Improved srgan for remote sensing image superresolution across locations and sensors," *Remote Sensing*, vol. 12, no. 8, p. 1263, 2020.

[21] W. Li, L. Fan, Z. Wang, C. Ma, and X. Cui, "Tackling mode collapse in multi-generator gans with orthogonal vectors," *Pattern Recognition*, vol. 110, p. 107646, 2020.

[22] Y. Hou and J. Zhang, "Unsupervised remote sensing image super-resolution method based on adaptive domain distance measurement network," in *2020 3rd International Conference on Advanced Electronic Materials, Computers and Software Engineering (AEMCSE)*. IEEE, 2020, pp. 256–259.

[23] W. Ma, Z. Pan, F. Yuan, and B. Lei, "Super-resolution of remote sensing images via a dense residual generative adversarial network," *Remote Sensing*, vol. 11, no. 21, p. 2578, 2019.

[24] K. Jiang, Z. Wang, P. Yi, J. Jiang, G. Wang, Z. Han, and T. Lu, "Gan-based multi-level mapping network for satellite imagery super-resolution," in *2019 IEEE International Conference on Multimedia and Expo (ICME)*. IEEE, Conference Proceedings, pp. 526–531.

[25] U. B. Gwali, S. T. Monteiro, and E. Saber, "Spectral super-resolution with optimized bands," *Remote Sensing*, vol. 11, no. 14, p. 1648, 2019.

[26] L. Zhu, Y. Chen, P. Ghamisi, and J. A. Benediktsson, "Generative adversarial networks for hyperspectral image classification," *IEEE Transactions on Geoscience and Remote Sensing*, vol. 56, no. 9, pp. 5046–5063, 2018.

[27] R. Jiang, X. Li, A. Gao, L. Li, H. Meng, S. Yue, and L. Zhang, "Learning spectral and spatial features based on generative adversarial network for hyperspectral image super-resolution," in *IGARSS 2019-*

- 1387 2019 *IEEE International Geoscience and Remote Sensing Symposium*.
1388 IEEE, Conference Proceedings, pp. 3161–3164.
- 1389 [28] J. Li, R. Cui, Y. Li, B. Li, Q. Du, and C. Ge, “Multitemporal
1390 hyperspectral image super-resolution through 3d generative adversarial
1391 network,” in *2019 10th International Workshop on the Analysis of
1392 Multitemporal Remote Sensing Images (MultiTemp)*. IEEE, 2019,
1393 Conference Proceedings, pp. 1–4.
- 1394 [29] Q. Huang, W. Li, T. Hu, and R. Tao, “Hyperspectral image super-
1395 resolution using generative adversarial network and residual learning,” in
1396 *ICASSP 2019-2019 IEEE International Conference on Acoustics, Speech
1397 and Signal Processing (ICASSP)*. IEEE, Conference Proceedings, pp.
1398 3012–3016.
- 1399 [30] G. Freedman and R. Fattal, “Image and video upscaling from local self-
1400 examples,” *ACM Transactions on Graphics (TOG)*, vol. 30, no. 2, pp.
1401 1–11, 2011.
- 1402 [31] W. Shi, J. Caballero, F. Huszár, J. Totz, A. P. Aitken, R. Bishop,
1403 D. Rueckert, and Z. Wang, “Real-time single image and video super-
1404 resolution using an efficient sub-pixel convolutional neural network,” in
1405 *Proceedings of the IEEE conference on computer vision and pattern
1406 recognition*, 2016, Conference Proceedings, pp. 1874–1883.
- 1407 [32] W.-S. Lai, J.-B. Huang, N. Ahuja, and M.-H. Yang, “Deep laplacian
1408 pyramid networks for fast and accurate super-resolution,” in *Proceedings
1409 of the IEEE conference on computer vision and pattern recognition*,
1410 Conference Proceedings, pp. 624–632.
- 1411 [33] A. Rangnekar, N. Mokashi, E. Ientilucci, C. Kanan, and M. Hoffman,
1412 “Aerial spectral super-resolution using conditional adversarial networks,”
1413 *arXiv preprint arXiv:1712.08690*, 2017.
- 1414 [34] P. Arun, K. M. Buddhiraju, A. Porwal, and J. Chanussot, “Cnn-
1415 based super-resolution of hyperspectral images,” *IEEE Transactions on
1416 Geoscience and Remote Sensing*, 2020.
- 1417 [35] G.-J. Qi, “Loss-sensitive generative adversarial networks on lipschitz
1418 densities,” *International Journal of Computer Vision*, pp. 1–23, 2019.
- 1419 [36] P. Samangouei, M. Kabkab, and R. Chellappa, “Defense-gan: Protecting
1420 classifiers against adversarial attacks using generative models,” *arXiv
1421 preprint arXiv:1805.06605*, 2018.
- 1422 [37] K. Liu, Q. Li, and G. Qiu, “Posegan: A pose-to-image translation
1423 framework for camera localization,” *ISPRS Journal of Photogrammetry
1424 and Remote Sensing*, vol. 166, pp. 308–315, 2020.
- 1425 [38] H. Zhang, J. Ma, C. Chen, and X. Tian, “Ndvi-net: A fusion network
1426 for generating high-resolution normalized difference vegetation index
1427 in remote sensing,” *ISPRS Journal of Photogrammetry and Remote
1428 Sensing*, vol. 168, pp. 182–196, 2020.
- 1429 [39] W. Jiang, Z. Liu, K.-H. Lee, S. Chen, Y.-L. Ng, Q. Dou, H.-C. Chang,
1430 and K.-W. Kwok, “Respiratory motion correction in abdominal mri using
1431 a densely connected u-net with gan-guided training,” *arXiv preprint
1432 arXiv:1906.09745*, 2019.
- 1433 [40] S. K. Yarlagadda, D. Güera, P. Bestagini, F. Maggie Zhu, S. Tubaro,
1434 and E. J. Delp, “Satellite image forgery detection and localization using
1435 gan and one-class classifier,” *Electronic Imaging*, vol. 2018, no. 7, pp.
1436 214–1, 2018.
- 1437 [41] A. Bhattacharjee, S. Banerjee, and S. Das, “Posix-gan: Generating multiple
1438 poses using gan for pose-invariant face recognition,” in *Proceedings
1439 of the European Conference on Computer Vision (ECCV)*, 2018, pp. 0–0.
- 1440 [42] X. Chen, C. Xu, X. Yang, and D. Tao, “Attention-gan for object trans-
1441 figuration in wild images,” in *Proceedings of the European Conference
1442 on Computer Vision (ECCV)*, 2018, pp. 164–180.
- 1443 [43] M. Zhang and Q. Ling, “Supervised pixel-wise gan for face super-
1444 resolution,” *IEEE Transactions on Multimedia*, 2020.
- 1445 [44] K. Lei, M. Qin, B. Bai, G. Zhang, and M. Yang, “Gcn-gan: A non-linear
1446 temporal link prediction model for weighted dynamic networks,” in
1447 *IEEE INFOCOM 2019-IEEE Conference on Computer Communications*.
1448 IEEE, 2019, pp. 388–396.
- 1449 [45] M. Cha, Y. Gwon, and H. Kung, “Adversarial nets with perceptual losses
1450 for text-to-image synthesis,” in *2017 IEEE 27th International Workshop
1451 on Machine Learning for Signal Processing (MLSP)*. IEEE, 2017, pp.
1452 1–6.
- 1453 [46] X. Luo, R. Chen, Y. Xie, Y. Qu, and C. Li, “Bi-gans-st for perceptual
1454 image super-resolution,” in *Proceedings of the European Conference on
1455 Computer Vision (ECCV)*, 2018, pp. 4–6.
- 1456 [47] Y. Blau and T. Michaeli, “The perception-distortion tradeoff,” in *Pro-
1457 ceedings of the IEEE Conference on Computer Vision and Pattern
1458 Recognition*, 2018, pp. 6228–6237.
- 1459 [48] M. S. Rad, B. Bozorgtabar, U.-V. Marti, M. Basler, H. K. Ekenel, and
1460 J.-P. Thiran, “Srobb: Targeted perceptual loss for single image super-
1461 resolution,” in *Proceedings of the IEEE International Conference on
1462 Computer Vision*, 2019, pp. 2710–2719.
- [49] P. Bojanowski, A. Joulin, D. Lopez-Paz, and A. Szlam, “Optimizing the
1463 latent space of generative networks,” *arXiv preprint arXiv:1707.05776*,
1464 2017. 1465
- [50] M. Arjovsky, S. Chintala, and L. Bottou, “Wasserstein generative ad-
1466 versarial networks,” ser. Proceedings of Machine Learning Research,
1467 D. Precup and Y. W. Teh, Eds., vol. 70. International Convention
1468 Centre, Sydney, Australia: PMLR, 06–11 Aug 2017, pp. 214–223. 1469
- [51] I. Gulrajani, F. Ahmed, M. Arjovsky, V. Dumoulin, and A. C. Courville,
1470 “Improved training of wasserstein gans,” in *Advances in neural infor-
1471 mation processing systems*, Conference Proceedings, pp. 5767–5777. 1472
- [52] L. Zhang, W. Wei, C. Bai, Y. Gao, and Y. Zhang, “Exploiting clustering
1473 manifold structure for hyperspectral imagery super-resolution,” *IEEE
1474 Transactions on Image Processing*, vol. 27, no. 12, pp. 5969–5982, 2018. 1475
- [53] L. Zhang, J. Nie, W. Wei, Y. Li, and Y. Zhang, “Deep blind hyperspectral
1476 image super-resolution,” *IEEE Transactions on Neural Networks and
1477 Learning Systems*, vol. 32, no. 6, pp. 2388–2400, 2020. 1478
- [54] S. Nah, T. Hyun Kim, and K. Mu Lee, “Deep multi-scale convolutional
1479 neural network for dynamic scene deblurring,” in *Proceedings of the
1480 IEEE conference on computer vision and pattern recognition*, 2017, pp.
1481 3883–3891. 1482
- [55] J. Cao and J. Wang, “Absolute exponential stability of recurrent neural
1483 networks with lipschitz-continuous activation functions and time delays,”
1484 *Neural networks*, vol. 17, no. 3, pp. 379–390, 2004. 1485
- [56] K. Zheng, L. Gao, W. Liao, D. Hong, B. Zhang, X. Cui, and J. Chanus-
1486 sot, “Coupled convolutional neural network with adaptive response
1487 function learning for unsupervised hyperspectral super resolution,” *IEEE
1488 Transactions on Geoscience and Remote Sensing*, vol. 59, no. 3, pp.
1489 2487–2502, 2020. 1490
- [57] R. Dian, S. Li, and L. Fang, “Learning a low tensor-train rank represen-
1491 tation for hyperspectral image super-resolution,” *IEEE transactions on
1492 neural networks and learning systems*, vol. 30, no. 9, pp. 2672–2683,
1493 2019. 1494
- [58] J. Li, R. Cui, B. Li, R. Song, Y. Li, Y. Dai, and Q. Du, “Hyperspectral
1495 image super-resolution by band attention through adversarial learning,”
1496 *IEEE Transactions on Geoscience and Remote Sensing*, 2020. 1497
- [59] S. Mei, X. Yuan, J. Ji, Y. Zhang, S. Wan, and Q. Du, “Hyperspectral
1498 image spatial super-resolution via 3d full convolutional neural network,”
1499 *Remote Sensing*, vol. 9, no. 11, p. 1139, 2017. 1500
- [60] A. Hore and D. Ziou, “Image quality metrics: Psnr vs. ssim,” in
1501 *2010 20th International Conference on Pattern Recognition*. IEEE,
1502 Conference Proceedings, pp. 2366–2369. 1503
- [61] S. S. Channappayya, A. C. Bovik, and R. W. Heath Jr, “Rate bounds
1504 on ssim index of quantized images,” *IEEE Transactions on Image
1505 Processing*, vol. 17, no. 9, pp. 1624–1639, 2008. 1506
- [62] Y. Blau, R. Mechrez, R. Timofte, T. Michaeli, and L. Zelnik-Manor,
1507 “The 2018 pirm challenge on perceptual image super-resolution,” in
1508 *Proceedings of the European Conference on Computer Vision (ECCV)*,
1509 Conference Proceedings, pp. 0–0. 1510
- [63] C. Ma, C.-Y. Yang, X. Yang, and M.-H. Yang, “Learning a no-reference
1511 quality metric for single-image super-resolution,” *Computer Vision and
1512 Image Understanding*, vol. 158, pp. 1–16, 2017. 1513
- [64] A. Mittal, R. Soundararajan, and A. C. Bovik, “Making a “completely
1514 blind” image quality analyzer,” *IEEE Signal Processing Letters*, vol. 20,
1515 no. 3, pp. 209–212, 2012. 1516
- [65] K. Liu, W. Tang, F. Zhou, and G. Qiu, “Spectral regularization for
1517 combating mode collapse in gans,” in *Proceedings of the IEEE/CVF
1518 International Conference on Computer Vision*, 2019, pp. 6382–6390. 1519
- [66] K. G. Hartmann, R. T. Schirrmeyer, and T. Ball, “Eeg-gan: Generative
1520 adversarial networks for electroencephalographic (eeg) brain signals,”
1521 *arXiv preprint arXiv:1806.01875*, 2018. 1522
- [67] J. Yang, Y. Zhao, C. Yi, and J. C.-W. Chan, “No-reference hyperspectral
1523 image quality assessment via quality-sensitive features learning,” *Remote
1524 Sensing*, vol. 9, no. 4, p. 305, 2017. 1525
- [68] G. Anbarjafari and H. Demirel, “Image super resolution based on
1526 interpolation of wavelet domain high frequency subbands and the spatial
1527 domain input image,” *ETRI journal*, vol. 32, no. 3, pp. 390–394, 2010. 1528
- [69] M. Srivastava, S. Pallavi, S. Chandra, and G. Geetha, “Comparison
1529 of optimizers implemented in generative adversarial network (gan),”
1530 *International Journal of Pure and Applied Mathematics*, vol. 119, no. 12,
1531 pp. 16 831–16 836, 2018. 1532